Isogeometric Bézier dual mortaring: the enriched Bézier dual basis with application to second- and fourth-order problems

Di Miao[1], Zhihui Zou[1], Michael A. Scott[1], Michael J. Borden[2], and Derek C. Thomas[2]

[1]Department of Civil and Environmental Engineering, Brigham Young University, Provo, UT USA
[2]Coreform LLC, Orem, UT USA

November 13, 2019

Abstract

In this paper, we present an algorithm to construct enriched Bézier dual basis functions that can reproduce higher-order polynomials. Our construction is unique in that it is based on Bézier extraction and projection, allowing it to be used for tensor product and unstructured polynomial spline spaces, is well-conditioned, and is quadrature-free. When used as a basis for dual mortar methods, optimal approximations are achieved for both second- and fourth-order problems. In the context of fourth-order problems, both C^0 and C^1 continuity constraints must be applied at each intersection. We develop a novel geometry-independent C^1 continuity constraint that also preserves the sparsity of the coupled problem. The performance of the proposed formulation is verified through several challenging second- and fourth-order problems.

1 Introduction

Isogeometric analysis, introduced by Hughes et al. [35], leverages computer aided design (CAD) representations directly in finite element analysis. It has been shown that this approach can alleviate the model preparation burden of going from a CAD design to an analysis model and improve overall solution accuracy and robustness [3, 20, 21]. Additionally, the higher-order smoothness inherent in CAD basis functions make it possible to solve higher-order partial differential equations such as the biharmonic equation [39, 38], the Kirchhoff-Love shell problem [41, 40, 42] and the Cahn-Hilliard equation [28, 9] directly without resorting to mixed discretization schemes.

CAD models are often built from collections of non-uniform rational B-splines (NURBS). Adjacent NURBS patches often have inconsistent knot layouts, different parameterizations, and may not even be physically connected. Additionally, trimming curves [43, 58] are often employed to further simplify the design process and to extend the range of objects that can be modeled by NURBS at the expense of further complicating the underlying parameterization of the object. While usually not an issue from a design perspective, these inconsistencies in the NURBS patch layout, including trimming, must be accommodated in the isogeometric model to achieve accurate simulation results. As shown in Figure 1, two primary approaches are often employed. First, the exact trimmed CAD model, shown in Figure 1 in the middle, is used directly in the simulation [58]. To accomplish this requires additional algorithms for handling cut cells and the weak imposition of boundary conditions and may result in reduced solution accuracy and robustness. Second, the CAD model is reparameterized [71], as shown in Figure 1 on the right, into a watertight spline representation like multi-patch NURBS, subdivision surfaces [55], or T-splines [62] which can then be used as a basis for analysis directly. The reparameterization process often results in more accurate and robust simulation results but is only semi-automatic using prevailing approaches. In both cases, existing techniques are primarily surface-based due to the predominance of surface-based CAD descriptions.

1.1 Key contributions

In the present work, we assume that some form of reparameterization has been performed (see Figure 1 on the right) on a CAD model to either remove some or all of the trimming curves and/or to restructure the underlying patch layout
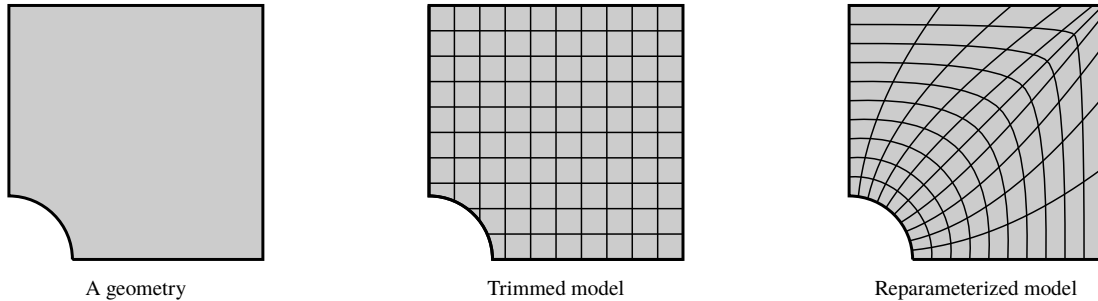
Figure 1: A geometry and two parameterization strategies: trimming and reparameterization.

to improve the parameterization (e.g., reduce degree, distortion, complexity, etc.). However, we relax the requirement that adjacent patches share a consistent parameterization along shared edges and instead introduce a dual mortaring along the shared interfaces. Relaxing this requirement can simplify the reparameterization process leading to more robust approaches [70]. Our key contributions include:

- The Bézier dual basis, introduced in [72], is enriched to be able to reproduce polynomials of any degree at the expense of a slight increase in the size of the underlying support.

- The polynomial enrichment is performed in a quadrature-free manner, resulting in well-conditioned dual basis functions, where the condition number is independent of mesh size.

- The approach is written entirely in terms of Bézier extraction, which means it can be applied equally to both tensor product and unstructured spline representations.

- For fourth-order problems, we introduce a geometry-independent C^1 continuity constraint. In other words, the constraint only depends on parametric information. Throughout this paper we call this C^1 constraint a dual mortar suitable constraint.

1.2 Prior work

The design and analysis communities have made significant progress in the representation and manipulation of complex CAD surfaces with nontrivial topology. In the design community, some of the earliest efforts resulted in the so-called subdvision surfaces [55, 15, 47] which allow for the construction of smooth spline bases over unstructured meshes. However, from an analysis perspective, subdivision surfaces are non-polynomial and require expensive numerical integration schemes [49] to achieve accuracy. Despite these challenges, Loop [52] and Catmull-Clark [66, 67, 14] subdivisions have been utilized in isogeometric analysis to generate and analyze smooth surfaces and solids.

T-splines [62], also introduced in the design community, are similar to subdivision surfaces in that they can be built over unstructured meshes but they also allow for local refinement. T-spline-based isogeometric analysis was first proposed in [2] and the approximation properties of so-called analysis-suitable T-splines was studied in [19]. T-splines have been widely applied in different areas including fracture [65], boundary element analysis [61], fluid-structure interaction [4] and shells [6].

The workhorse of modern CAD is the boundary representation (BREP). This term most often refers to a collection of NURBS patches together with trimming data that defines how a patch is to be trimmed down and topological data giving the connection between patches. A BREP in which all the patches are untrimmed is often referred to as a multi-patch NURBS object.

One of the most difficult aspects of building smooth CAD models from multi-patch NURBS objects is achieving smoothness and approximability in the neighborhood of extraordinary points [64]. In a surface, an extraordinary point is a vertex in the mesh which has more or less than four adjacent edges. The concept of geometric smoothness has been used extensively in the construction of smooth surfaces over extraordinary points [26] and some of these concepts have been utilized in the context of isogeometric analysis [61, 53, 54].

In [39], geometric smoothness was also used to construct C^1 smooth functions on two-patch planar domains and multi-patch planar domains [38]. A possible issue with this approach is so-called C^1 locking [18]. In [16], a local degree

elevation approach is proposed to overcome this form of locking and is applied to the construction of geometrically continuous functions on smooth surfaces.

From the analysis perspective, the pointwise satisfaction of continuity constraints between adjacent patches is often unnecessarily rigorous. A reasonable approximation can be achieved even if these constraints are applied in a variational setting. For this reason, various variational approaches have been proposed to weakly couple disconnected patches, including the Lagrange multiplier method [25, 31, 33, 11], the penalty method [40, 1], the discontinuous Galerkin method [57, 50, 32] and the mortar method [7, 5, 68, 8, 72, 68].

The mortar method, first introduced by Bernardi [7], considers a constrained solution space and gives rise to a positive definite variational problem. While the discontinuous Galerkin method requires modifications to weak forms, the mortar method modifies function spaces, leaving weak forms untouched. Mortar methods, in the context of isogeometric analysis, have been studied in [13] and later extended to address the C^1 continuity constraint for Kirchhoff-Love shells [59] and C^n continuity coupling [24]. Recently, a hybrid approach, which combines mortar and penalty methods, was developed for fourth-order problems in a multi-patch setting [34]. In [68], dual basis functions are used to discretize the Lagrange multiplier space, which further simplifies the mortar formulation.

Dual functionals for splines were first introduced by de Boor and Fix [23] to develop a quasi-interpolation operator for splines. Subsequently, de Boor presented dual basis functions in [22]. Thomas et al. [63] introduced the Bézier projection operator as an efficient replacement for global L^2 projection. The dual basis induced by the Bézier projection operator has been utilized in [48, 72] to alleviate locking and for patch coupling. In the finite element framework, the construction of dual basis functions with optimal approximation power was first presented in [51]. In [45], Lamichhane and Wohlmuth [44] introduced locally supported and continuous dual basis functions for quadratic finite elements. Later on, Lamichhane and Wohlmuth developed a class of dual basis functions that have the same support as the corresponding nodal finite element basis and possess adequate approximation power.

Recently, Wunderlich et al. [69] extended the dual mortar formulation in [51] to isogeometric analysis. However, the construction algorithm in [51] calls the assembly routine twice – once to construct a dual basis with minimal support and a second time to the enrich the dual basis with polynomial completeness. Moreover, the condition number of the series of linear problems solved in [51] grows at the rate p as the mesh is refined.

The remainder of the paper is organized as follows: In Section 2, required notation is established including closed forms for the Gramian of the Bernstein basis, its inverse, and the inner product between the Bernstein basis and polynomials. Bézier extraction is also presented. Section 3 discusses the mathematical requirements for enriched dual basis functions with optimal approximation power. A quadrature-free algorithm for building enriched Bézier dual basis functions is then presented in Section 4. An overview of the dual mortar formulation is given in Section 5. In Section 6, we describe how the enriched Bézier dual basis can be incorporated into a dual mortar formulation for second-order problems. A dual mortar suitable C^1 constraint and corresponding dual mortar formulation for fourth-order problems are then described in Section 7. Section 8 demonstrates the utility of the approach for several second- and fourth-order numerical benchmarks. Conclusions are drawn in Section 9.

2 Spline fundamentals

2.1 The univariate Bernstein basis

The ith univariate Bernstein basis function of degree p on the unit interval $[0, 1]$ is defined by

$$B_i^p(\xi) = \binom{p}{i} \xi^i (1 - \xi)^{p-i} \tag{1}$$

where the binomial coefficient $\binom{p}{i} = \dfrac{p!}{i!(p-i)!}$, $0 \le i \le p$. The polynomial degree superscript will be omitted when unnecessary. Matrix-vector notation will be used throughout, with bold fonts indicating matrices and vectors, e.g., the vector form of a set of Bernstein basis functions is denoted by

$$\mathbf{B}^p(\xi) = \begin{bmatrix} B_0^p(\xi) \\ B_1^p(\xi) \\ \vdots \\ B_p^p(\xi) \end{bmatrix}. \tag{2}$$

3

The Bernstein basis of degree p spans the space of polynomials of degree p. The Gramian matrix $\mathbf{G}^p = [G_{i,j}^p]$ can be given as an integral

$$G_{i,j}^p = \int_0^1 B_i^p(\xi) B_j^p(\xi) d\xi, \tag{3}$$

or in closed form (see [27]) as

$$G_{i,j}^p = \frac{\binom{p}{i}\binom{p}{j}}{(2p+1)\binom{2p}{i+j}}. \tag{4}$$

The inverse of the Gramian matrix is given in closed form (see [37]) as

$$[G_{i,j}^p]^{-1} = \frac{(-1)^{i+j}}{\binom{p}{i}\binom{p}{j}} \sum_{k=0}^{\min(i,j)} \binom{p+k+1}{p-i}\binom{p-k}{p-i}\binom{p+k+1}{p-j}\binom{p-k}{p-j}. \tag{5}$$

A Bernstein basis defined over an arbitrary interval $\left[\xi_\alpha, \xi_\beta\right]$ can be evaluated as

$$B_i^p\left(\frac{\xi - \xi_\alpha}{\xi_\beta - \xi_\alpha}\right), \qquad \xi \in \left[\xi_\alpha, \xi_\beta\right]. \tag{6}$$

The corresponding scaled Gramian and inverse can be obtained by multiplying and dividing the matrices in Eq. (4) and Eq. (5) by the scaling factor $(\xi_\beta - \xi_\alpha)$, respectively. For the sake of simplicity, we use the same symbols to represent the Bernstein basis defined on different intervals. A closed form expression for the L^2 inner product between the Bernstein basis function $B_i^p(\xi)$ and a polynomial ξ^j is given by

$$\int_0^1 B_i^p(\xi) \xi^j d\xi = \binom{p}{i} \frac{(i+j)!(p-i)!}{(p+j+1)!}. \tag{7}$$

2.2 The univariate B-spline basis

A set of univariate B-spline basis functions of degree p can be uniquely defined by a non-decreasing knot vector $\Xi = \{\xi_i\}_{i=0}^{n+p}$, where n is the number of B-spline basis functions. In this work, we only use open knot vectors where the first and last values in the knot vector is repeated $p+1$ times i.e., $\xi_0 = \xi_1 = \cdots = \xi_p$ and $\xi_n = \xi_{n+1} = \cdots = \xi_{n+p}$ defined over the interval $[0,1]$. The value of the ith B-spline basis function associated with the knot vector Ξ is recursively defined using the Cox-de Boor formula

$$N_i^0(\xi) = \begin{cases} 1 & \xi_i \le \xi \le \xi_{i+1} \\ 0 & \text{otherwise} \end{cases} \tag{8}$$

$$N_i^p(\xi) = \frac{\xi - \xi_i}{\xi_{i+p} - \xi_i} N_i^{p-1}(\xi) + \frac{\xi_{i+p+1} - \xi}{\xi_{i+p+1} - \xi_{i+1}} N_{i+1}^{p-1}(\xi). \tag{9}$$

Non-uniform rational B-splines (NURBS) are often used to represent conic sections. A NURBS basis function can be written as

$$R_i^p(\xi) = \frac{N_i^p(\xi) w_i}{W(\xi)} \tag{10}$$

where the positive number w_i is the weight corresponding to basis function N_i^p and

$$W(\xi) = \sum_j N_j^p(\xi) w_j. \tag{11}$$

2.3 Bézier extraction

Bézier extraction is a technique that is often used to facilitate the incorporation of smooth splines into existing finite element codes [10, 60]. The Bézier element extraction operator $\mathbf{C}^e$ maps a Bernstein basis vector $\mathbf{B}^e$ defined over an element Ω_e to a corresponding B-spline basis vector $\mathbf{N}$ restricted to the same element. In other words,

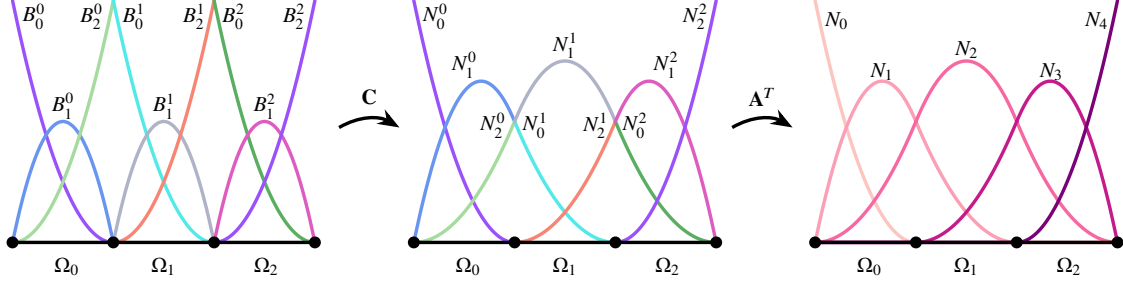$$\mathbf{N}^e := \mathbf{N}|_{\Omega_e} = \mathbf{C}^e \mathbf{B}^e. \tag{12}$$

Figure 2: The Bézier extraction process for a quadratic B-spline basis defined by the knot vector $\{0, 0, 0, 1/3, 2/3, 1, 1, 1\}$.

In the context of tensor product B-splines, the Bézier extraction operator can be constructed through a knot insertion algorithm [56]. The inverse of the Bézier element extraction operator $\mathbf{R}^e := [\mathbf{C}^e]^{-1}$ is called the spline element reconstruction operator and is used in the construction of the Bézier projection operator (see [63]).

It is possible to interpret Bézier extraction as a global assembly procedure. The B-spline basis vector $\mathbf{N}$ of dimension n_N can be represented as

$$\mathbf{N} = \mathbf{A}^T \mathbf{C} \mathbf{B}, \tag{13}$$

where the vector of Bernstein bases over all elements in the mesh is a vector of dimension $n_B = (p+1)n_e$ given by

$$\mathbf{B} = \begin{bmatrix} \mathbf{B}^1 \\ \mathbf{B}^2 \\ \vdots \\ \mathbf{B}^{n_e} \end{bmatrix} \tag{14}$$

and $\mathbf{C}$ is a block $n_B \times n_B$ diagonal matrix with Bézier element extraction operators on the diagonal and the rectangular assembly operator $\mathbf{A}$ is the permutation matrix that maps element degrees of freedom to global degrees of freedom. The assembly operator $\mathbf{A}$ satisfies the following properties:

- Each row of $\mathbf{A}$ contains a single unity-valued entry; all other entries are zero.

- Each column of $\mathbf{A}$ contains at most $p+1$ unity-valued entries; all other entries are zero.

- Compact support. The non-zero entries can be associated to no more than $p+1$ consecutive elements.

- If we consider the column vectors $\mathbf{A}_i$ of $\mathbf{A}$, the space $\mathsf{span}\{\mathbf{A}_i\}_{i=0}^{n_N-1}$ is an n_N dimensional subspace of $\mathbb{R}^{n_B}$ and $\{\mathbf{A}_i\}_{i=0}^{n_N-1}$ are orthogonal, i.e.

$$\mathbf{A}_i \cdot \mathbf{A}_j \neq 0 \iff i = j. \tag{15}$$

The Bézier extraction process for the quadratic B-spline basis defined by the knot vector $\{0, 0, 0, 1/3, 2/3, 1, 1, 1\}$ is shown in Fig. 2. The assembly operator $\mathbf{A}$ for this example is given by

$$\mathbf{A} = \begin{array}{c} \begin{array}{ccccc} N_0 & N_1 & N_2 & N_3 & N_4 \end{array} \\ \begin{bmatrix} 1 & 0 & 0 & 0 & 0 \\ 0 & 1 & 0 & 0 & 0 \\ 0 & 0 & 1 & 0 & 0 \\ 0 & 1 & 0 & 0 & 0 \\ 0 & 0 & 1 & 0 & 0 \\ 0 & 0 & 0 & 1 & 0 \\ 0 & 0 & 1 & 0 & 0 \\ 0 & 0 & 0 & 1 & 0 \\ 0 & 0 & 0 & 0 & 1 \end{bmatrix} \end{array} \begin{array}{c} N_0^0 \\ N_1^0 \\ N_2^0 \\ N_0^1 \\ N_1^1 \\ N_2^1 \\ N_0^2 \\ N_1^2 \\ N_2^2 \end{array}, \tag{16}$$

where the highlighted submatrix is the restriction of $\mathbf{A}$ onto elements Ω_0 and Ω_1 and onto the B-spline basis functions N_1 and N_2.
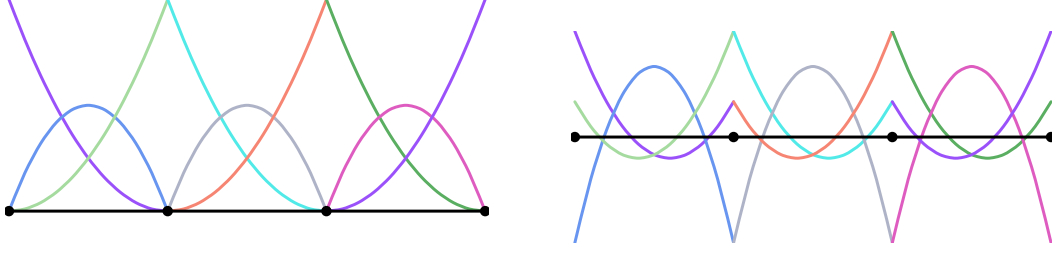
Figure 3: A Bernstein basis (left) and the corresponding dual basis (right) for degree $p = 2$ defined over the knot vector $\{0, 0, 0, 1/3, 2/3, 1, 1, 1\}$. Note that each dual basis function has the same support as the corresponding primal basis function.

2.4 The tensor product B-spline basis and extraction operator

A common way to extend Bernstein, B-spline, and NURBS basis functions to higher dimensions is by constructing the tensor product of univariate basis functions. For example, a two-dimensional Bernstein basis of degree $\mathbf{p} = (p_\xi, p_\eta)$ can be defined as

$$\mathbf{B}^{\mathbf{p}}(\xi, \eta) = \mathbf{B}^{p_\xi}(\xi) \otimes \mathbf{B}^{p_\eta}(\eta). \tag{17}$$

The Kronecker product of an $m \times n$ matrix $\mathbf{A}$ and a $p \times q$ matrix $\mathbf{B}$ is a $mp \times nq$ block matrix defined as

$$\mathbf{A} \otimes \mathbf{B} = \begin{bmatrix} a_{11}\mathbf{B} & \cdots & a_{1n}\mathbf{B} \\ \vdots & \ddots & \vdots \\ a_{m1}\mathbf{B} & \cdots & a_{mn}\mathbf{B} \end{bmatrix}. \tag{18}$$

In the tensor product setting, the Gramian of the Bernstein basis and the Bézier element extraction operator can be written as

$$\mathbf{G}^{\mathbf{p}} = \mathbf{G}^{p_\xi} \otimes \mathbf{G}^{p_\eta}, \tag{19}$$

and

$$\mathbf{C}^{\mathbf{p}} = \mathbf{C}^{p_\xi} \otimes \mathbf{C}^{p_\eta}, \tag{20}$$

respectively. Since the inverse of the Kronecker product of matrices is simply the Kronecker product of the inverses, the inverse of the multivariate Gramian $\mathbf{G}^{\mathbf{p}}$ is given by

$$[\mathbf{G}^{\mathbf{p}}]^{-1} = [\mathbf{G}^{p_\xi}]^{-1} \otimes [\mathbf{G}^{p_\eta}]^{-1}, \tag{21}$$

and the reconstruction matrix

$$\mathbf{R}^{\mathbf{p}} := [\mathbf{C}^{\mathbf{p}}]^{-1} = [\mathbf{C}^{p_\xi}]^{-1} \otimes [\mathbf{C}^{p_\eta}]^{-1} = \mathbf{R}^{p_\xi} \otimes \mathbf{R}^{p_\eta}. \tag{22}$$

2.5 Dual basis functions

2.5.1 Bernstein dual basis functions

For a Bernstein basis $\mathbf{B}$, a dual basis $\hat{\mathbf{B}}$ can be formulated by simply using the inverse Gramian as

$$\hat{\mathbf{B}} := \mathbf{G}^{-1}\mathbf{B}. \tag{23}$$

A graphical depiction of a Bernstein basis and the corresponding dual basis is shown in Figure 3. Importantly, the Bernstein dual basis is locally supported and each dual basis has the same support as the corresponding primal basis function, i.e., $\mathrm{supp}\,\hat{B}_i = \mathrm{supp}\,B_i$. Additionally, the space spanned by the dual basis (denoted by $\mathcal{B}$) is the same as the space spanned by the primal Bernstein basis (denoted by $\hat{\mathcal{B}}$).

2.5.2 B-spline dual basis functions

For a B-spline basis $\mathbf{N}$, a dual basis $\hat{\mathbf{N}}$ can be formulated abstractly as

$$\langle \hat{N}_i, N_j \rangle_\Omega := \int_\Omega \hat{N}_i N_j d\Omega = \delta_{ij}. \tag{24}$$

We denote the spans of $\mathbf{N}$ and $\hat{\mathbf{N}}$ by $\mathcal{N}, \hat{\mathcal{N}} \subset \mathcal{B}$, respectively. We can also introduce a pair of quasi-interpolation operators

$$\mathcal{I}_\mathcal{N} u = \sum_i \langle \hat{N}_i, u \rangle_\Omega N_i, \text{ and } \mathcal{I}_{\hat{\mathcal{N}}} u = \sum_i \langle N_i, u \rangle_\Omega \hat{N}_i, \tag{25}$$

where both $\mathcal{I}_\mathcal{N}$ and $\mathcal{I}_{\hat{\mathcal{N}}}$ are projection operators, i.e., for all $u \in \mathcal{N}$, $v \in \hat{\mathcal{N}}$, $\mathcal{I}_\mathcal{N} u = u$ and $\mathcal{I}_{\hat{\mathcal{N}}} v = v$.

The construction of a B-spline dual basis with the same properties as the Bernstein dual basis, i.e., compact support and polynomial completeness, is challenging. A general B-spline dual basis construction procedure can be written in terms of Bézier extraction.

Lemma 1. *$\hat{\mathbf{N}} \subset \mathcal{B}$ is dual to $\mathbf{N} \subset \mathcal{B}$ if and only if*

$$\hat{\mathbf{N}} = \mathbf{W}^T \mathbf{R}^T \mathbf{G}^{-1} \mathbf{B} = \mathbf{W}^T \mathbf{R}^T \hat{\mathbf{B}}, \tag{26}$$

where the weighted assembly matrix $\mathbf{W}^T$ is a pseudo-inverse of $\mathbf{A}$, i.e., $\mathbf{W}^T \mathbf{A} = \mathbf{I}$.

Proof. Given a basis vector in the form of Equation (26), its inner product with the spline basis vector is given by

$$\langle \hat{\mathbf{N}}, \mathbf{N}^T \rangle_\Omega = \mathbf{W}^T \mathbf{R}^T \langle \hat{\mathbf{B}}, \mathbf{B}^T \rangle_\Omega \mathbf{C}^T \mathbf{A} = \mathbf{I}. \tag{27}$$

On the other hand, we assume that $\hat{\mathbf{N}}$ is dual to $\mathbf{N}$. With the help of a quasi-interpolation operator $\mathcal{I}_\mathcal{B} u = \sum_i \langle \hat{B}_i, u \rangle_\Omega B_i$ in $\mathcal{B}$, we can rewrite the basis vector $\hat{\mathbf{N}}$ in terms of $\hat{\mathbf{B}}$ as

$$\hat{\mathbf{N}} = \tilde{\mathbf{W}}^T \hat{\mathbf{B}}, \text{ with } \tilde{W}_{i,j} = \langle \hat{B}_i, \hat{N}_j \rangle_\Omega. \tag{28}$$

Hence, one can rewrite $\hat{\mathbf{N}}$ in the form of Equation (26), with $\mathbf{W} = \mathbf{C}\tilde{\mathbf{W}}$ and $\mathbf{W}^T \mathbf{A} = \mathbf{I}$. □

We can now see that the construction of a compactly supported dual basis can be simplified to finding a set of banded vectors $\{\mathbf{W}_i\}_{i=0}^{n_N-1}$ such that

$$\mathbf{W}_i \cdot \mathbf{A}_j = \delta_{ij}. \tag{29}$$

The support size of a dual basis constructed from Equation (26) is determined by the bandwidth of $\mathbf{W}$. The weighting scheme [63], proposed for Bézier projection, has been adopted to construct $\mathbf{W}$ for the Bézier dual basis in [48, 72]. The Bézier dual basis has compact support and can be used to reduce locking [48, 29], and as a dual mortaring strategy for elasticity problems [72].

A dual basis function constructed with Bézier projection is show in Figure 4c for the quadratic B-spline shown in Figure 4a. Note that the Bézier dual basis function has the same compact support as the primal B-spline basis function. For comparison, a global dual basis function constructed by inverting the B-spline Gramian matrix is shown in Figure 4b. Notice that the global dual basis function has global support.

3 The approximation power of dual bases

In most cases, a locally constructed quasi-interpolation operator $\mathcal{I}_\mathcal{N}$ possesses optimal approximation power. However, without special care, a locally constructed dual quasi-interpolation operator $\mathcal{I}_{\hat{\mathcal{N}}}$ possesses suboptimal approximation power. In fact, for any degree it usually provides an approximation accuracy of only $O(h)$. This is due to the fact that the dual basis underlying $\mathcal{I}_{\hat{\mathcal{N}}}$ often lacks polynomial completeness. To demonstrate this, we approximate the global Legendre polynomials using the Bézier dual basis constructed with Bézier projection. Figure 5 shows the results for a degree three dual basis over a two element domain. There are significant discrepancies between the dual basis approximations and the corresponding polynomials for all Legendre polynomials except the constant function.

In addition to the application of the dual basis as a local functional for the quasi-interpolation operator $\mathcal{I}_\mathcal{N}$, the dual basis is also widely used to solve constrained finite element problems. The advantage of using a dual basis as the
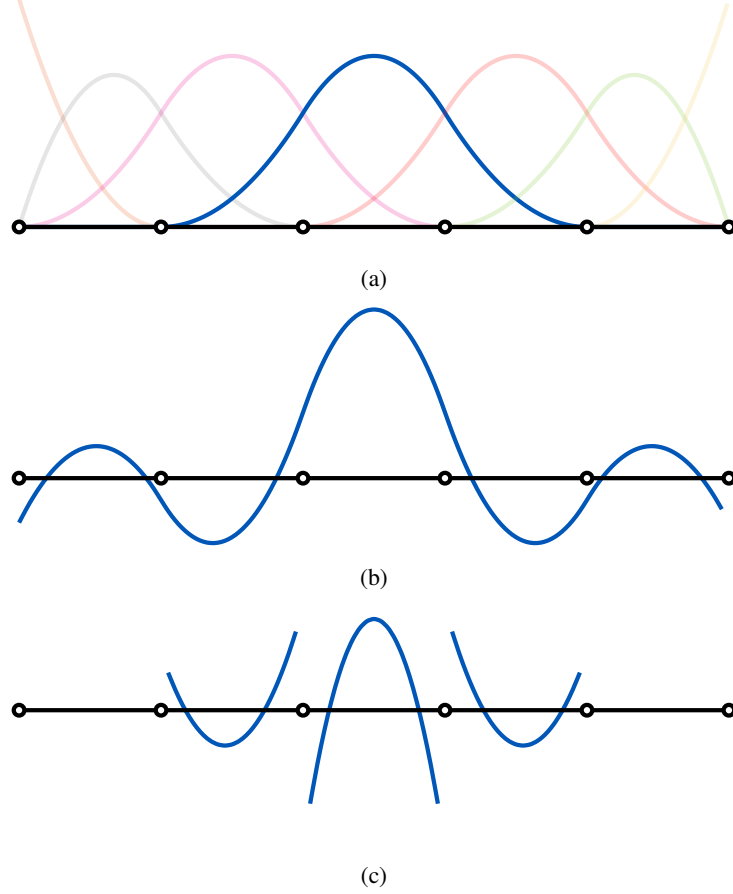
Figure 4: A comparison of a quadratic C^1 B-spline basis function (a) and the corresponding global dual basis function (b) and the Bézier dual basis function constructed with Bézier projection (c).

Lagrange multiplier is that the degrees of freedom associated with the multiplier can be locally condensed out leading to sparse, positive-definite linear systems.

However, the best finite element approximation of the Lagrange multiplier method is governed by the approximation power of the Lagrange multiplier. This means that, when a conventional dual basis is used to define the Lagrange multiplier space, the approximation power of the Lagrange multiplier does not improve as the polynomial degree is increased.

3.1 Theoretical motivation

In this section, we discuss the theoretical properties that a dual basis must satisfy to improve the approximation power to a given order.

Property 1. *(global idempotence) The dual quasi-interpolation operator $\mathcal{I}_{\hat{N}}$ preserves polynomials of degree q on the entire domain, i.e.,*

$$\mathcal{I}_{\hat{N}}p = p, \quad \forall p \in \mathcal{P}^q(\Omega). \tag{30}$$

Property 2. *(compact support) Each dual basis function $\hat{N}_i$ is supported by at most m connected elements and* $\operatorname{supp} N_i \subset \operatorname{supp} \hat{N}_i$.

Property 3. *(local stability) The restriction of the dual quasi-interpolation operator $\mathcal{I}_{\hat{N}}$ on Ω_e is bounded, i.e.,*

$$\|\mathcal{I}_{\hat{N}}u\|_{H^k(\Omega_e)} \le C_{st}\|u\|_{H^k(\hat{\Omega}_e)}, \tag{31}$$

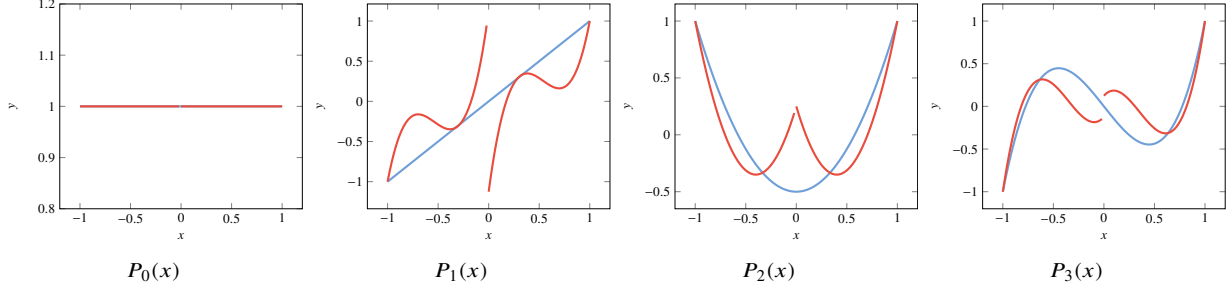*where C_{st} is a constant independent of h and will be defined later.*

Figure 5: The Legendre polynomials (——) and the corresponding best L^2 approximations (——) by degree 3 order Bézier dual basis functions defined on a two element domain. Bézier dual basis functions can only replicate the constant function.

From Property 1 and Property 2, we have the following result:

Lemma 2. *(local idempotence) For each element $\Omega_e \subset \Omega$, there is an extension element $\hat{\Omega}_e$ comprised of a fixed number of connected elements such that*

$$\left(\mathcal{I}_{\hat{N}} p\right)|_{\Omega_e} = p, \quad \forall p \in \mathcal{P}^q(\hat{\Omega}_e). \tag{32}$$

Proof. We define

$$\hat{\Omega}_e = \begin{cases} \bigcup_{i=0}^{e+m-1} \Omega_i, & e-m+1 < 0 \\ \bigcup_{i=e-m+1}^{n_e-1} \Omega_i, & e+m-1 > n_e - 1 \\ \bigcup_{i=e-m+1}^{e+m-1} \Omega_i, & \text{otherwise,} \end{cases} \tag{33}$$

where n_e is the number of elements in Ω. Since each $\hat{N}_i$ is supported by at most m connected elements, if $\Omega_e \subset \operatorname{supp} \hat{N}_i$, then $\operatorname{supp} \hat{N}_i \subset \hat{\Omega}_e$ and the evaluation $\langle N_i, p \rangle$ in (25) can be done in $\hat{\Omega}_e$, owing to $\operatorname{supp} N_i \subset \operatorname{supp} \hat{N}_i$. Hence, local polynomial preservation can be obtained from the global idempotence for polynomials. □

We now state the approximation properties of a polynomial space $\mathcal{P}$, the proof of which can be found in [12].

Lemma 3. *(Bramble-Hilbert) Let Ω be star-shaped and $Q^q u$ be the Taylor polynomial of order q of $u \in H^{q+1}(\Omega)$, then*

$$|u - Q^q u|_{H^k(\Omega)} \leq C_{bh} h^{q+1-k} |u|_{H^{q+1}(\Omega)}, \quad k = \{0, 1, \ldots, q+1\}, \tag{34}$$

where h is the diameter of Ω and C_{bh} is a constant independent of h.

Using the Bramble-Hilbert lemma, local idempotence, and local stability, we can state the convergence behavior of the dual quasi-interpolation operator $\mathcal{I}_{\hat{N}}$.

Theorem 1. *Let k and m be integer indices with $0 \leq k \leq m \leq q+1$ and $u \in H^m(\hat{\Omega}_e)$. Then for $0 \leq k \leq m$, we have*

$$\|u - \mathcal{I}_{\hat{N}} u\|_{H^k(\Omega_e)} \leq C h^{m-k} \|u\|_{H^m(\hat{\Omega}_e)}, \tag{35}$$

where C is a constant independent of h.

Proof. $\forall p \in \mathcal{P}^q(\hat{\Omega}_e)$, we have

$$\begin{aligned} \|u - \mathcal{I}_{\hat{N}} u\|_{H^k(\Omega_e)} &\leq \|u - p\|_{H^k(\Omega_e)} + \|p - \mathcal{I}_{\hat{N}} u\|_{H^k(\Omega_e)} \\ &= \|u - p\|_{H^k(\Omega_e)} + \|\mathcal{I}_{\hat{N}}(p - u)\|_{H^k(\Omega_e)} \\ &\leq (1 + C_{st}) \|u - p\|_{H^k(\hat{\Omega}_e)}, \end{aligned} \tag{36}$$

by choosing $p = Q^q u$, we have

$$\|u - \mathcal{I}_{\hat{N}} u\|_{H^k(\Omega_e)} \leq (1 + C_{st}) \|u - Q^q u\|_{H^k(\hat{\Omega}_e)} \leq C_{bh}(1 + C_{st}) h^{m-k} \|u\|_{H^m(\hat{\Omega}_e)}. \tag{37}$$

□

Hence, in order for the dual quasi-interpolation operator $\mathcal{I}_{\hat{N}}$ to converge at a given rate t, $\mathcal{I}_{\hat{N}}$ must preserve polynomials on the entire domain up to degree $t-1$. In addition, the compact support and local stability requirements must be satisfied. In the next section, we will construct a dual basis that satisfies Property 1 and explain how the construction procedure ensures the satisfaction of Property 2 and Property 3.

9

4 Embedding polynomials into the dual basis function space

We now describe how to construct a set of enriched dual basis functions which will endow $\mathcal{I}_{\hat{\mathcal{N}}}$ with polynomial reproduction up to a given degree. The construction is a two-step procedure:

1. For a given assembly matrix $\mathbf{A}$, we find a set of sparse vectors $\{\mathbf{W}_i^{\text{ini}}\}_{i=0}^{n_N-1}$ such that $\mathbf{W}_i^{\text{ini}} \cdot \mathbf{A}_j = \delta_{ij}$. Its matrix form $\mathbf{W}^{\text{ini}}$ will be taken to be the initial guess for the assembly matrix $\mathbf{W}$ of the desired dual basis.

2. The column vectors of $\mathbf{W}^{\text{ini}}$ are then modified by vectors $\{\mathbf{W}_i^{\text{mod}}\}_{i=0}^{n_N-1}$ which come from the null space of $\text{span}\{\mathbf{A}_i\}_{i=0}^{n_N-1}$ until polynomial reproduction is fulfilled. Note that this modification will maintain the biorthogonal relation between $\{\mathbf{W}_i\}_{i=0}^{n_N-1}$ and $\{\mathbf{A}_i\}_{i=0}^{n_N-1}$ where

$$\mathbf{W}_i = \mathbf{W}_i^{\text{ini}} + \mathbf{W}_i^{\text{mod}}. \tag{38}$$

4.1 An orthonormal basis for the space $\mathbb{R}^{n_B}$

To facilitate the construction of the enriched dual basis, we build a set of orthonormal vectors which form a basis for $\mathbb{R}^{n_B}$. Each orthonormal vector will have minimal support, where the support of a vector is taken to be the distance between the first and last nonzero entry. Since the column vectors $\mathbf{A}_i$ of $\mathbf{A}$ are orthogonal to each other, a natural choice for this basis is given by the set of vectors comprising all of the normalized $\{\mathbf{A}_i\}_{i=0}^{n_N-1}$, denoted by $\{\bar{\mathbf{A}}_i\}_{i=0}^{n_N-1}$, and the vectors which span the null space of $\text{span}\{\mathbf{A}_i\}_{i=0}^{n_N-1}$, denoted by $\{\mathbf{A}_i^{\perp}\}_{i=0}^{n_B-n_N-1}$. Note that the nonzero entries of any $\{\mathbf{A}_i\}_{i=0}^{n_N-1}$ are unity-valued. In addition, each row of $\mathbf{A}$ contains one unity-valued entry.

The vectors $\{\mathbf{A}_i^{\perp}\}_{i=0}^{n_B-n_N-1}$ can be found by constructing vectors which are orthonormal to every vector in $\{\bar{\mathbf{A}}_i\}_{i=0}^{n_N-1}$ from $\mathbb{R}^{n_i}$, where n_i is the number of nonzero entries in $\bar{\mathbf{A}}_i$. Note that each $\mathbf{A}_i^{\perp}$ can be used to construct a function in $\mathcal{B}$ as

$$\tilde{N}_i = \left[\mathbf{A}_i^{\perp}\right]^T \mathbf{CB}. \tag{39}$$

Since $\{\bar{\mathbf{A}}_i\}_{i=0}^{n_N-1}$ and $\{\mathbf{A}_i^{\perp}\}_{i=0}^{n_B-n_N-1}$ span the space $\mathbb{R}^{n_B}$, $\{N_i\}_{i=0}^{n_N-1}$ and $\{\tilde{N}_i\}_{i=0}^{n_B-n_N-1}$ span the space $\mathcal{B}$. Algorithm 1 can be used to efficiently construct the basis vectors $\{\mathbf{A}_i^{\perp}\}_{i=0}^{n_B-n_N-1}$.

Algorithm 1: An algorithm to compute $\{\mathbf{A}_i^{\perp}\}_{i=0}^{n_B-n_N-1}$ with minimum support such that $\{\{\bar{\mathbf{A}}_i\}_{i=0}^{n_N-1}, \{\mathbf{A}_i^{\perp}\}_{i=0}^{n_B-n_N-1}\}$ spans $\mathbb{R}^{n_B}$.

    Input   : $\{\mathbf{A}_i\}_{i=0}^{n_N-1}$

    Output   : A set of orthonormal basis vectors $\{\mathbf{A}_i^{\perp}\}_{i=0}^{n_B-n_N-1}$ for the null space of $\text{span}\{\mathbf{A}_i\}_{i=0}^{n_N-1}$

1 $j = 0$;

2 Initialize $\{\mathbf{A}_i^{\perp}\}_{i=0}^{n_B-n_N-1}$ with zero vectors of size n_B;

3 **for** $i = 0, 1, \ldots, n_N - 1$ **do**

4 nz = the number of nonzero entries of $\mathbf{A}_i$;

5   **if** $nz > 1$ **then**

6   **for** $k = 1, \ldots, nz - 1$ **do**

7   Map each entry of $[\underbrace{1, \ldots, 1}_{k}, -k]$ to $\mathbf{A}_j^{\perp}$ according to the indices of the nonzero entries of $\mathbf{A}_i$;

8   normalize $\mathbf{A}_j^{\perp}$ by $\mathbf{A}_j^{\perp} = \dfrac{\mathbf{A}_j^{\perp}}{|\mathbf{A}_j^{\perp}|}$;

9 $j = j + 1$;

10   **end**

11   **end**

12 **end**

For example, using the assembly matrix $\mathbf{A}$ shown in (16) as input, we can construct the following set of basis vectors

with Algorithm 1:

$$
\left\{
\underbrace{
\begin{bmatrix}1\\0\\0\\0\\0\\0\\0\\0\end{bmatrix},
\begin{bmatrix}0\\1/\sqrt{2}\\0\\1/\sqrt{2}\\0\\0\\0\\0\end{bmatrix},
\begin{bmatrix}0\\0\\1/\sqrt{3}\\0\\1/\sqrt{3}\\0\\1/\sqrt{3}\\0\end{bmatrix},
\begin{bmatrix}0\\0\\0\\0\\0\\1/\sqrt{2}\\0\\1/\sqrt{2}\end{bmatrix},
\begin{bmatrix}0\\0\\0\\0\\0\\0\\0\\1\end{bmatrix}
}_{\{\bar{\mathbf{A}}_i\}_{i=0}^{n_N-1}},
\underbrace{
\begin{bmatrix}0\\1/\sqrt{2}\\0\\-1/\sqrt{2}\\0\\0\\0\\0\end{bmatrix},
\begin{bmatrix}0\\0\\1/\sqrt{2}\\0\\-1/\sqrt{2}\\0\\0\\0\end{bmatrix},
\begin{bmatrix}0\\0\\1/\sqrt{6}\\0\\1/\sqrt{6}\\0\\-2/\sqrt{6}\\0\end{bmatrix},
\begin{bmatrix}0\\0\\0\\0\\0\\1/\sqrt{2}\\0\\-1/\sqrt{2}\end{bmatrix}
}_{\{\mathbf{A}_i^{\perp}\}_{i=0}^{n_B-n_N-1}}
\right\}.
\tag{40}
$$

4.2 Constructing an initial guess $\mathbf{W}_i^{\text{ini}}$

An initial guess $\mathbf{W}_i^{\text{ini}}$ for $\mathbf{W}$ can be constructed simply as

$$
\mathbf{W}_i^{\text{ini}} = \mathbf{A}_i/n_i,
\tag{41}
$$

where n_i is the number of nonzero entries in $\mathbf{A}_i$. As will be seen in the next section, this initial guess is critical for finding an appropriate $\mathbf{W}^{\text{mod}}$ with the desired polynomial reproduction property.

4.3 Polynomial reproduction

We now establish an appropriate $\mathbf{W}^{\text{mod}}$ such that the quasi-interpolation operator $\mathcal{I}_{\hat{N}}$ reproduces a polynomial vector $\mathbf{P} = [1, \xi, \ldots, \xi^q]^T$ $(q \le p)$. In other words,

$$
\mathcal{I}_{\hat{N}}(\mathbf{P}) = \mathbf{P}.
\tag{42}
$$

Since both the dual basis function space $\hat{N}$ and the polynomial space are subspaces of the piecewise Bernstein space $\mathcal{X}$, Equation (42) can be verified through the variational problem

$$
\langle v, \mathcal{I}_{\hat{N}}(\mathbf{P}^T)\rangle_\Omega = \langle v, \mathbf{P}^T\rangle_\Omega, \quad \forall v \in \mathcal{X}.
\tag{43}
$$

Replacing $\mathcal{I}_{\hat{N}}$ in Equation (43) by its definition (Equation (25)) and expressing v in Bernstein form, we have

$$
\langle \mathbf{B}, \hat{\mathbf{N}}^T\rangle_\Omega \langle \mathbf{N}, \mathbf{P}^T\rangle_\Omega = \langle \mathbf{B}, \mathbf{P}^T\rangle_\Omega
$$
$$
\mathbf{R}\mathbf{W}\langle \mathbf{N}, \mathbf{P}^T\rangle_\Omega = \langle \mathbf{B}, \mathbf{P}^T\rangle_\Omega
\tag{44}
$$
$$
\mathbf{W}^{\text{ini}}\langle \mathbf{N}, \mathbf{P}^T\rangle_\Omega + \mathbf{W}^{\text{mod}}\langle \mathbf{N}, \mathbf{P}^T\rangle_\Omega = \mathbf{C}\langle \mathbf{B}, \mathbf{P}^T\rangle_\Omega
$$

where the vector form of the B-spline basis $\mathbf{N}$ may be replaced by its Bézier extraction form, i.e.,

$$
\mathbf{W}^{\text{ini}}\mathbf{A}^T \mathbf{C}\langle \mathbf{B}, \mathbf{P}^T\rangle_\Omega + \mathbf{W}^{\text{mod}}\mathbf{A}^T \mathbf{C}\langle \mathbf{B}, \mathbf{P}^T\rangle_\Omega = \mathbf{C}\langle \mathbf{B}, \mathbf{P}^T\rangle_\Omega.
\tag{45}
$$

Using the initial guess defined in Equation (41) we have

$$
\mathbf{W}^{\text{ini}}\mathbf{A}^T = \bar{\mathbf{A}}(\bar{\mathbf{A}})^T,
\tag{46}
$$

where $\bar{\mathbf{A}}$ is the matrix form of $\{\bar{\mathbf{A}}_i\}_{i=0}^{n_N-1}$. The operator $\bar{\mathbf{A}}(\bar{\mathbf{A}})^T : \mathbb{R}^{n_B} \to \mathsf{span}\{\bar{\mathbf{A}}_i\}_{i=0}^{n_N-1}$ is an l^2-projection operator for any vector in $\mathbb{R}^{n_B}$. Hence, owing to the direct sum decompostion

$$
\mathbb{R}^{n_B} = \mathsf{span}\{\bar{\mathbf{A}}_i\}_{i=0}^{n_N-1} \oplus \mathsf{span}\{\mathbf{A}_i^{\perp}\}_{i=0}^{n_B-n_N-1}.
\tag{47}
$$

Equation (45) is equivalent to

$$
\mathbf{W}^{\text{ini}}\mathbf{A}^T \mathbf{C}\langle \mathbf{B}, \mathbf{P}^T\rangle_\Omega + \mathbf{W}^{\text{mod}}\mathbf{A}^T \mathbf{C}\langle \mathbf{B}, \mathbf{P}^T\rangle_\Omega = \bar{\mathbf{A}}(\bar{\mathbf{A}})^T \mathbf{C}\langle \mathbf{B}, \mathbf{P}^T\rangle_\Omega + \mathbf{A}^{\perp}(\mathbf{A}^{\perp})^T \mathbf{C}\langle \mathbf{B}, \mathbf{P}^T\rangle_\Omega,
\tag{48}
$$
$$
\mathbf{W}^{\text{mod}}\mathbf{A}^T \mathbf{C}\langle \mathbf{B}, \mathbf{P}^T\rangle_\Omega = \mathbf{A}^{\perp}(\mathbf{A}^{\perp})^T \mathbf{C}\langle \mathbf{B}, \mathbf{P}^T\rangle_\Omega,
\tag{49}
$$

where $\mathbf{A}^{\perp}$ is the matrix form of $\{\mathbf{A}_i^{\perp}\}_{i=0}^{n_B-n_N-1}$, or

$$
\left(\mathbf{A}_i^{\perp}\right)^T \mathbf{W}^{\text{mod}}\langle \mathbf{N}, \mathbf{P}^T\rangle_\Omega = \left(\mathbf{A}_i^{\perp}\right)^T \mathbf{C}\langle \mathbf{B}, \mathbf{P}^T\rangle_\Omega = \langle \tilde{N}_i, \mathbf{P}^T\rangle_\Omega, \quad i \in \{0, 1, \ldots, n_B - n_N - 1\}.
\tag{50}
$$

Remark 1. *Obviously,* $\mathbf{A}^{\perp}(\mathbf{A}^{\perp})^T : \mathbb{R}^{n_B} \to \text{span}\{\mathbf{A}_i^{\perp}\}_{i=0}^{n_B-n_N-1}$ *is an l^2-projection operator in $\mathbb{R}^{n_B}$ with unity norm* $\|\mathbf{A}^{\perp}\mathbf{A}^{\perp T}\| = 1$. *Additionally, vectors* $\{\mathbf{W}_i^{mod}\}_{i=0}^{n_N-1} \in \text{span}\{\mathbf{A}_i^{\perp}\}_{i=0}^{n_B-n_N-1}$, *which ensures that the modification made by* $\mathbf{W}^{mod}$ *will not influence the biorthogonal relation between* $\mathbf{W}$ *and* $\mathbf{A}$.

We now develop an efficient algorithm to compute a modification matrix $\mathbf{W}^{\text{mod}}$ that satisfies Equation (50). The resulting modification matrix will be as banded as possible and the zero entries in $\mathbf{W}^{\text{mod}}$ will remain zero in $\mathbf{W}$. In other words, there are no new nonzero entries introduced by the sum of $\mathbf{W}^{\text{mod}}$ and $\mathbf{W}^{\text{ini}}$.

Algorithm 2: An algorithm to construct $\mathbf{W}^{\text{mod}}$.

> **Input** : $\{\mathbf{A}_i^{\perp}\}_{i=0}^{n_B-n_N-1}$, polynomial degree q
> **Output** : $\mathbf{W}^{\text{mod}}$

1 Initialize $\mathbf{P} = [1, \xi, \ldots, \xi^q]^T$;
2 Initialize $\mathbf{W}^{\text{mod}} = \mathbf{0}_{n_B \times n_N}$;
3 Assemble the matrix $\mathbf{C}\langle \mathbf{B}, \mathbf{P}^T \rangle_{\Omega}$, $\langle \mathbf{N}, \mathbf{P}^T \rangle_{\Omega}$ may then be obtained via the assembly operator $\mathbf{A}$;
4 **for** $i = 0, 1, \ldots, n_B - n_N - 1$ **do**
5 $\quad$ *ind* = the index of the vector $\mathbf{A}_{ind}$ that is used to construct $\mathbf{A}_i^{\perp}$ in Algorithm 1 (shares the same nonzero entries as $\mathbf{A}_i^{\perp}$);
6 $\quad$ Find $q+1$ indices $\{n_0, n_1, \ldots, n_q\}$ that are closest to *ind* and $0 \le n_0 \le n_q \le n_N - 1$;
7 $\quad$ Define a square matrix $\mathbf{M}$ from the $\{n_0, n_1, \ldots, n_q\}$ columns of $\langle \mathbf{P}, \mathbf{N}^T \rangle_{\Omega}$;
8 $\quad$ Construct a vector $\mathbf{F} = \langle \mathbf{P}, \tilde{N}_i \rangle_{\Omega}$ from $\mathbf{C}\langle \mathbf{B}, \mathbf{P}^T \rangle_{\Omega}$ and Equation (39);
9 $\quad$ Solve $\mathbf{X} = \mathbf{M}^{-1}\mathbf{F}$;
10 $\quad$ **for** $j = 0, 1, \ldots, q$ **do**
11 $\quad\quad$ $\mathbf{W}_{n_j}^{\text{mod}} = \mathbf{W}_{n_j}^{\text{mod}} + x_j \mathbf{A}_i^{\perp}$;
12 $\quad$ **end**
13 **end**

The procedure for constructing the matrix $\mathbf{W}^{\text{mod}}$ is given in Algorithm 2. The functions that are involved in one iteration of Algorithm 2 for constructing a quadratic dual basis that reproduces quadratic polynomials are shown in Figure 6. For a vector $\mathbf{A}_i^{\perp}$, one can construct a basis function $\tilde{N}_i$ of $\mathcal{X}$ by Equation (39) (Figure 6a). Since $\mathbf{A}_i^{\perp}$ is constructed by $\mathbf{A}_{11}$ from Algorithm 1, $[\langle \mathbf{P}, N_{10} \rangle_{\Omega}]$, $[\langle \mathbf{P}, N_{11} \rangle_{\Omega}]$ and $[\langle \mathbf{P}, N_{12} \rangle_{\Omega}]$ are selected to form the matrix $\mathbf{M}$ (highlighted in Figure 6b). A consequence of this approach is that the support of each dual basis function consists of no more than $p+q+1$ elements. Although the support is slightly enlarged through the modification procedure, it still remains local. The domain involved in the formulation of $\mathbf{M}$ is $[s, e]$, highlighted by orange blocks. The polynomials involved in the formulation of $\mathbf{M}$ and $\mathbf{F}$ are highlighted in Figure 6c.

4.4 A robust quadrature-free algorithm to construct enriched dual basis functions with polynomial reproduction

Although Algorithm 2 builds locally supported dual basis functions that preserve polynomials, the use of polynomials defined on the entire domain $[0, 1]$ in Equation (42) can be troublesome due to near linear dependencies that can develop as the mesh is refined. The fundamental issue is illustrated in Figure 6c. To overcome this issue, we can modify the approach to use localized polynomials in each iteration. Consider the linear map

$$F = \frac{\xi - s}{e - s} : [s, e] \to [0, 1]. \tag{51}$$

Replacing $\mathbf{P}$ by $\mathbf{P} \circ F = [1, t \circ F, \ldots, t^q \circ F]^T$ (see Figure 6d) in Algorithm 2, both spline basis functions and $\mathbf{P} \circ F$ are refined as the mesh is refined. As a result, the condition number of $\mathbf{M}$, constructed from $\mathbf{P} \circ F$, will not deteriorate as the mesh is refined. $\mathbf{P} \circ F$ can be constructed from $\mathbf{P}$ through an affine mapping operator $\mathbf{T}$ as

$$\mathbf{P} \circ F = \mathbf{TP}. \tag{52}$$

For the example shown in Figure 6, the operator $\mathbf{T}$ is given by

$$\mathbf{T} = \begin{bmatrix} 1 & 0 & 0 \\ \dfrac{-s}{e-s} & \dfrac{1}{e-s} & 0 \\ \left(\dfrac{-s}{e-s}\right)^2 & \dfrac{-2s}{(e-s)^2} & \dfrac{1}{(e-s)^2} \end{bmatrix}. \tag{53}$$

Hence, the two linear systems are essentially the same with the operator $\mathbf{T}$ acting as a pre-conditioner that improves the conditioning of the matrix $\mathbf{M}$ in Algorithm 2. A general algorithm that computes the affine mapping operator $\mathbf{T}$: $\mathbf{T}\mathbf{P} \circ F_1 = \mathbf{P} \circ F_2$, with $F_1 = \frac{\xi - s_1}{e_1 - s_1}$ and $F_2 = \frac{\xi - s_2}{e_2 - s_2}$ is given in Algorithm 3.

Algorithm 3: An affine mapping operator $\mathbf{T}$: $\mathbf{T}\mathbf{P} \circ F_1 = \mathbf{P} \circ F_2$.

Input	: The highest polynomial degree q, $\{s_1, e_1\}$ and $\{s_2, e_2\}$
Output	: Matrix form of operator $\mathbf{T}$

1 Compute $s = \dfrac{s_2 - s_1}{e_1 - s_1}$ and $e = \dfrac{e_2 - s_1}{e_1 - s_1}$;

2 Initialize $\mathbf{T}_{q \times q}$;

3 **for** $j = 0, 1, \ldots, q$ **do**

4 $\quad$ **for** $i = 0, 1, \ldots, j$ **do**

5 $\quad\quad$ $T_{i,j} = \binom{j}{i} \dfrac{(-s)^{j-i}}{(e-s)^j}$

6 $\quad$ **end**

7 **end**

Another issue with Algorithm 2 is the need to call a matrix assembly routine during the construction of the matrix $\mathbf{C}\langle \mathbf{B}, \mathbf{P}^T \rangle_\Omega$. Leveraging the Bézier element extraction operator, the affine mapping operator, and the closed form expression of the inner product between Bernstein basis functions and polynomials, we can develop a quadrature-free formulation for the enriched Bézier dual basis. The procedure is given in Algorithm 4.

Algorithm 4: A quadrature-free algorithm to construct $\mathbf{W}^{\text{mod}}$.

Input	: $\{\mathbf{A}_i^\perp\}_{i=0}^{n_B - n_N - 1}$, polynomial degree q
Output	: $\mathbf{W}^{\text{mod}}$

1 Initialize $\mathbf{W}^{\text{mod}} = \mathbf{0}_{n_B \times n_N}$;

2 Initialize $\mathbf{P} = [1, \xi, \ldots, \xi^q]^T$;

3 Initialize $\mathbf{D} = \int_0^1 \mathbf{B}\mathbf{P}^T d\xi$ by Equation (7);

4 **for** $i = 0, 1, \ldots, n_B - n_N - 1$ **do**

5 $\quad$ ind = the index of the vector $\mathbf{A}_{ind}$ that is used to construct $\mathbf{A}_i^\perp$ in Algorithm 1 (shares the same nonzero entries as $\mathbf{A}_i^\perp$);

6 $\quad$ Find $q + 1$ indices $\{n_0, n_1, \ldots, n_q\}$ that are the closest to ind and $0 \le n_0 \le n_q \le n_N - 1$, and identify involved elements;

7 $\quad$ Construct the block diagonal matrix $\tilde{\mathbf{D}}$ from the matrix $\mathbf{D}$. The submatrices on the diagonal correspond to the inner product between Bernstein basis functions and piecewise polynomials on each element ;

8 $\quad$ Construct $\tilde{\mathbf{T}}$ from Algorithm 3 (see Figure 7a), $\tilde{\mathbf{C}}$ by restricting the extraction operator $\mathbf{C}$ to the involved elements, $\tilde{\mathbf{A}}$ by restricting the assembly operator $\mathbf{A}$ to the involved elements and B-spline basis functions, and $\tilde{\mathbf{A}}_i^\perp$ by restricting $\mathbf{A}_i^\perp$ to the involved elements (see Figure 7b);

9 $\quad$ Construct $\mathbf{M} = \tilde{\mathbf{T}}^T \tilde{\mathbf{D}}^T \tilde{\mathbf{C}}^T \tilde{\mathbf{A}}$ and $\mathbf{F} = \tilde{\mathbf{T}}^T \tilde{\mathbf{D}}^T \tilde{\mathbf{C}}^T \tilde{\mathbf{A}}_i^\perp$;

10 $\quad$ Solve $\mathbf{X} = \mathbf{M}^{-1}\mathbf{F}$;

11 $\quad$ **for** $j = 0, 1, \ldots, q$ **do**

12 $\quad\quad$ $\mathbf{W}_{n_j}^{\text{mod}} = \mathbf{W}_{n_j}^{\text{mod}} + x_j \mathbf{A}_i^\perp$;

13 $\quad$ **end**
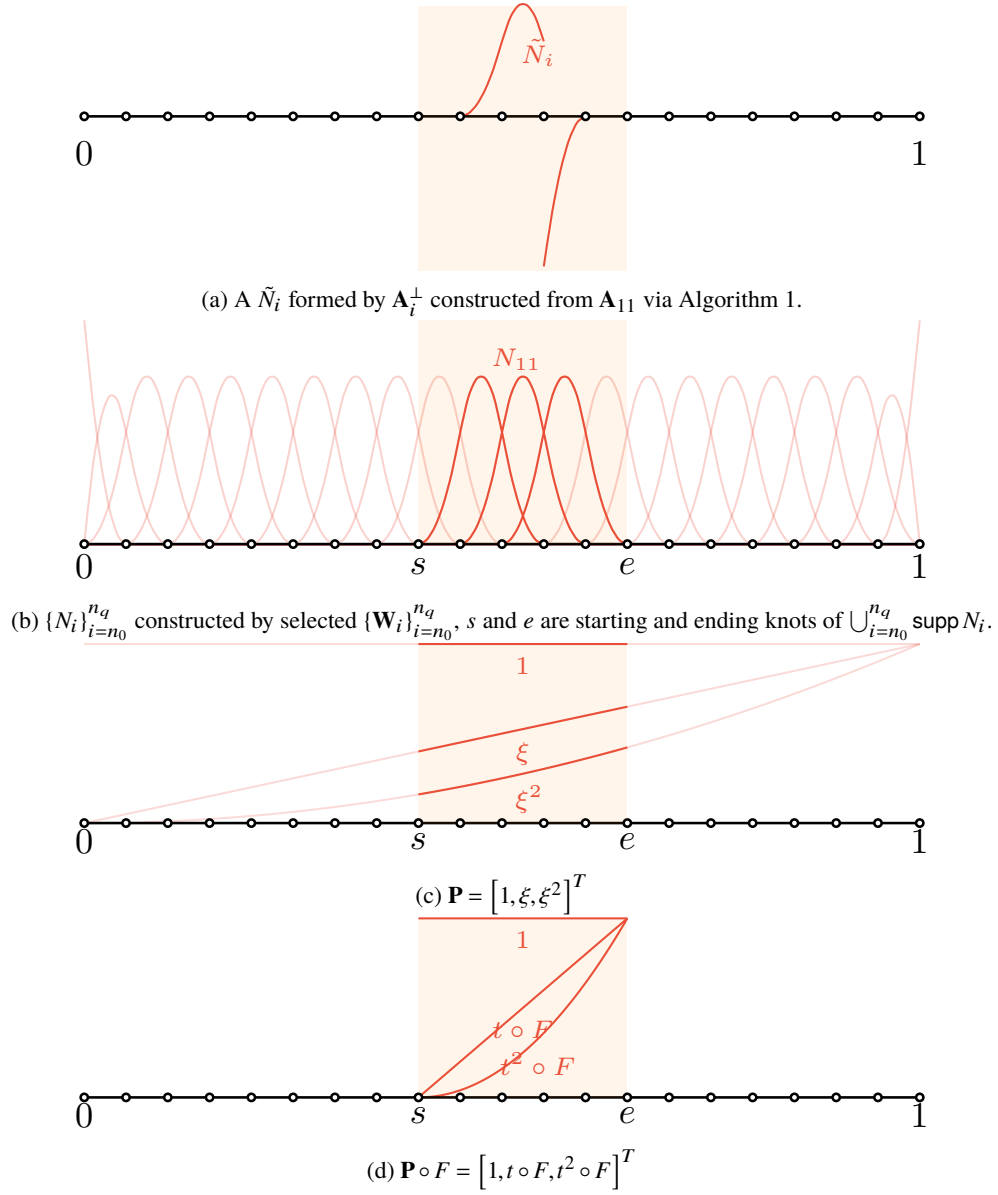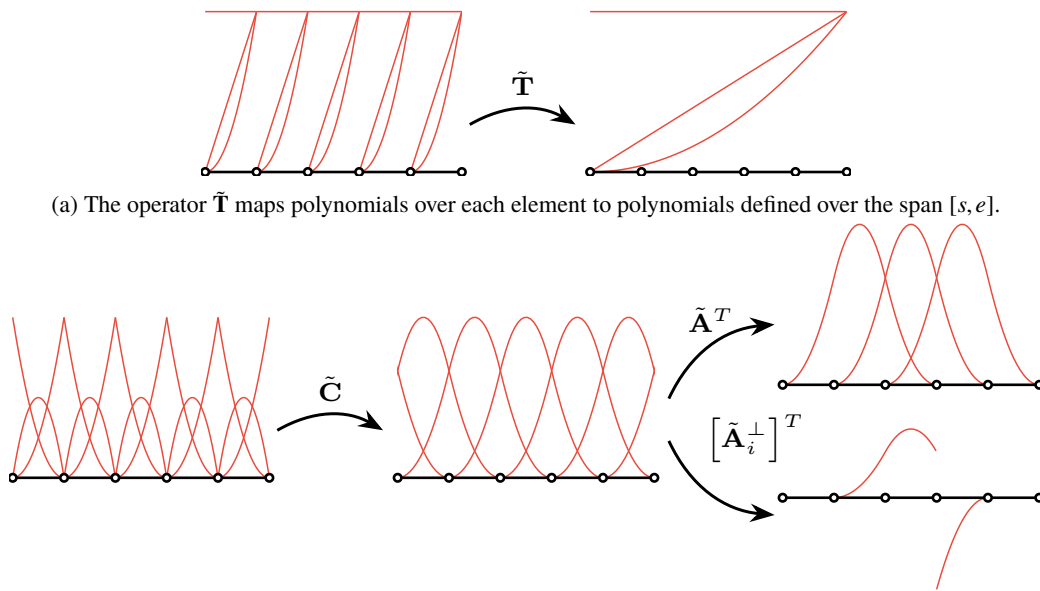
14 **end**

(a) A $\tilde{N}_i$ formed by $\mathbf{A}_i^{\perp}$ constructed from $\mathbf{A}_{11}$ via Algorithm 1.

(b) $\{N_i\}_{i=n_0}^{n_q}$ constructed by selected $\{\mathbf{W}_i\}_{i=n_0}^{n_q}$, s and e are starting and ending knots of $\bigcup_{i=n_0}^{n_q} \operatorname{supp} N_i$.

(c) $\mathbf{P} = \left[1, \xi, \xi^2\right]^T$

(d) $\mathbf{P} \circ F = \left[1, t \circ F, t^2 \circ F\right]^T$

Figure 6: Illustration of all involved basis functions, polynomials and elements in one iteration of Algorithm 2 and Algorithm 4.

(a) The operator $\tilde{\mathbf{T}}$ maps polynomials over each element to polynomials defined over the span $[s, e]$.

(b) The block diagonal matrix $\tilde{\mathbf{C}}$ maps Bernstein basis functions to discontinuous B-spline basis functions, the assembly operator $\tilde{\mathbf{A}}$ constructed by restricting the operator $\mathbf{A}$ to the involved elements and spline basis functions maps discontinuous spline basis functions to continuous spline basis functions, and the operator $\tilde{\mathbf{A}}_i^{\perp}$ constructed by restricting the operator $\mathbf{A}_i^{\perp}$ to the involved elements maps discontinuous spline basis functions to functions $\tilde{N}_i$.

Figure 7: Illustration of the behavior of the operators used in Algorithm 4.

A comparison of the maximum condition numbers of the matrices $\mathbf{M}$ produced by Algorithm 2 and Algorithm 4, respectively, for constructing p^{th} order dual basis functions with p^{th} order polynomial reproduction ($q = p$) is shown in Figure 8. As can be seen, the condition number of $\mathbf{M}$ from Algorithm 2 grows at the rate p, whereas the condition number of $\mathbf{M}$ from Algorithm 4 is independent of mesh refinement. These results indicate that Algorithm 4 has the desired robustness.
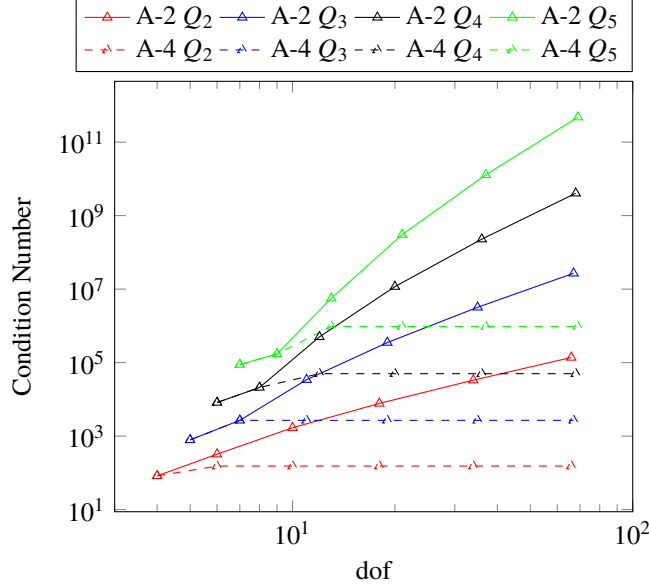
Figure 8: The growth of the maximum condition numbers of the matrix $\mathbf{M}$ produced by Algorithm 2 and Algorithm 4.

Leveraging Algorithm 2 and Algorithm 4, the enriched dual basis reproduces global polynomials (Property 1), and the construction process guarantee that the support of each enriched dual basis function consists of no more than $p + q + 1$ elements (Property 2). It remains to prove the local stability property (Property 3).

Proof of Property 3.

$$
\begin{aligned}
\|\mathcal{I}_{\hat{N}} u\|_{H^k(\Omega_e)} &= \| \sum_i \langle N_i, u \rangle_\Omega \hat{N}_i \|_{H^k(\Omega_e)} \\
&\leq \| \sum_i \hat{N}_i \|_{H^k(\Omega_e)} \|\langle \mathbf{N}, u \rangle_{\hat{\Omega}_e} \|_\infty \\
&= \|\hat{\mathbf{N}}^T \mathbf{1}\|_{H^k(\Omega_e)} \|\langle \mathbf{N}, u \rangle_{\hat{\Omega}_e} \|_\infty,
\end{aligned}
\tag{54}
$$

where $\mathbf{1}$ is a unit valued vector of the same size as $\hat{\mathbf{N}}$. By rewriting $\hat{\mathbf{N}}$ in its expanded form (26), we have

$$
\|\mathcal{I}_{\hat{N}} u\|_{H^k(\Omega_e)} \leq \| \sum_i B_i \|_{H^k(\Omega_e)} \|\mathbf{G}^{-T}\mathbf{R}\mathbf{W}\mathbf{1}\|_\infty \|\langle \mathbf{N}, u \rangle_{\hat{\Omega}_e} \|_\infty.
\tag{55}
$$

From the definition of matrix norms, we then have

$$
\begin{aligned}
\|\mathcal{I}_{\hat{N}} u\|_{H^k(\Omega_e)} &\leq \| \sum_i B_i \|_{H^k(\Omega_e)} \|\mathbf{G}^{-T}\mathbf{R}\mathbf{W}\|_\infty \|\langle \mathbf{N}, u \rangle_{\hat{\Omega}_e} \|_\infty \\
&\leq \| \sum_i B_i \|_{H^k(\Omega_e)} \|\mathbf{G}^{-T}\|_\infty \|\mathbf{R}\|_\infty \|\mathbf{W}\|_\infty \|\langle \mathbf{N}, u \rangle_{\hat{\Omega}_e} \|_\infty.
\end{aligned}
\tag{56}
$$

Since the Bernstein basis forms a partition of unity over each element, we have that

$$
\| \sum_i B_i \|_{H^k(\Omega_e)} = \|1\|_{H^k(\Omega_e)} = \|1\|_{L^2(\Omega_e)} = \sqrt{h}.
\tag{57}
$$

16

Let $\mathbf{G}_{[0,1]}$ be the Gramian matrix defined on the interval $[0,1]$ and assume $\|\mathbf{G}_{[0,1]}^{-1}\|_{\infty} = C_{gi}$, we have

$$\|\mathbf{G}^{-T}\|_{\infty} = \|\mathbf{G}^{-1}\|_{\infty} = h^{-1}\|\mathbf{G}_{[0,1]}^{-1}\|_{\infty} = C_{gi}h^{-1}. \tag{58}$$

Owing to the fact that the Bézier element extraction operators are independent of the geometry and are invariant under uniform scaling, their norms are independent of the mesh size. In addition, there are a finite number of different Bézier element extraction operators generated by uniform mesh refinement. Hence, we can assume $\|\mathbf{R}\|_{\infty} = C_r$. Meanwhile, thanks to Algorithm 4, the construction of $\mathbf{W}$ is geometry and mesh size independent. Hence, we can assume that $\|\mathbf{W}\|_{\infty} = C_w$.

Since spline basis functions are non-negative and also form a partition of unity, from Lemma 2 and the Cauchy-Schwarz inequality, we have that

$$\|\langle \mathbf{N}, u \rangle_{\hat{\Omega}_e}\|_{\infty} \leq \|\langle \mathbf{1}, u \rangle_{\hat{\Omega}_e}\|_{\infty} = |\int_{\hat{\Omega}_e} u d\Omega| \leq \|1\|_{L^2(\hat{\Omega}_e)}\|u\|_{L^2(\hat{\Omega}_e)} = \sqrt{C_m h}\|u\|_{L^2(\hat{\Omega}_e)} \tag{59}$$

where C_m is the number of elements involved in $\hat{\Omega}_e$. By substituting Equations (57), (58), and (59) into Equation (56), we have that

$$\begin{aligned}
\|\mathcal{I}_{\hat{\mathcal{N}}} u\|_{H^k(\Omega_e)} &\leq C_{gi} C_w C_r \sqrt{C_m}\|u\|_{L^2(\hat{\Omega}_e)} \\
&\leq C_{gi} C_w C_r \sqrt{C_m}\|u\|_{H^k(\hat{\Omega}_e)}.
\end{aligned} \tag{60}$$

This concludes the proof with $C_{st} = C_{gi} C_w C_r \sqrt{C_m}$. $\qquad\square$

Hence, the enriched dual basis satisfies all required technical properties and will yield optimal approximations. Figure 9 gives an example of enriched Bézier dual basis functions of the same primal B-spline basis function with different polynomial reproduction orders. As can be seen, the approximation power is improved at the expense of the support size. Due to the tensor product structure of multivariate spline basis functions, the proposed approach can be directly extended to higher dimensional spaces via tensor product.

5 The dual mortar method for multi-patch coupling

5.1 Domain decomposition

Let Ω be a bounded open domain in $\mathbb{R}^2$ with its boundary denoted by $\partial\Omega$. We assume that Ω can be subdivided into K non-overlapping patches Ω_k for $1 \leq k \leq K$, i.e.,

$$\bar{\Omega} = \bigcup_{k=1}^{K} \bar{\Omega}_k \quad \text{and} \quad \Omega_k \bigcap \Omega_l = \emptyset, \quad \forall k \neq l \tag{61}$$

where $\bar{\Omega}_k$ is the closure of Ω_k. For simplicity, we only consider the case where the intersection of two patches is either empty, a single vertex, or the entire edge. We denote the common interface of two neighboring patches as $\Gamma_{kl} = \partial\Omega_k \bigcap \partial\Omega_l$ so that $\Gamma_{kl} = \emptyset$ if Ω_k is not a neighbor of Ω_l. We also define the skeleton $\mathbf{S} = \bigcup_{k,l \in K, k<l} \Gamma_{kl}$ as the union of all interfaces in Ω. For each interface $\Gamma \in \mathbf{S}$, one adjacent subdomain is considered to be slave $\Omega_s(\Gamma)$ while the other is considered as master $\Omega_m(\Gamma)$. The set $\mathbf{V}$ denotes the set of all vertices in Ω. A representative example of a multi-patch geometry is shown in Figure 10.

For each patch, there exists a bijective geometric mapping from the parametric domain $\hat{\Omega}_k$ to the physical domain Ω_k, which is defined as

$$\mathbf{F}_k(\xi_k, \eta_k) : \hat{\Omega}_k \mapsto \Omega_k \in \mathbb{R}^2, \tag{62}$$

where (ξ_k, η_k) are the coordinates of the parametric domain. For simplicity and without loss of generality, we assume the parametric domain is $\hat{\Omega}_k = [0,1] \times [0,1]$ for all patches.

We can use the mappings $\mathbf{F}_k$ to create connections between neighboring patches. Due to the fact that $\mathbf{F}_k$ is a bijection, there exists an inverse mapping denoted by $\mathbf{F}_k^{-1}$. We can construct a bijective transformation on the intersection Γ_{kl} as

$$\mathbf{E}_{kl} = \mathbf{F}_l^{-1} \circ \mathbf{F}_k, \tag{63}$$

which maps a parametric point on $\partial\hat{\Omega}_k \bigcap \hat{\Gamma}_{kl}$ to a physical point on the intersection Γ_{kl} and then to a parametric point on $\partial\hat{\Omega}_l \bigcap \hat{\Gamma}_{kl}$.

(a) A cubic B-spline function

(b) Bézier dual basis function

(c) Enriched Bézier dual basis function that reproduces linear functions

(d) Enriched Bézier dual basis function that reproduces quadratic functions

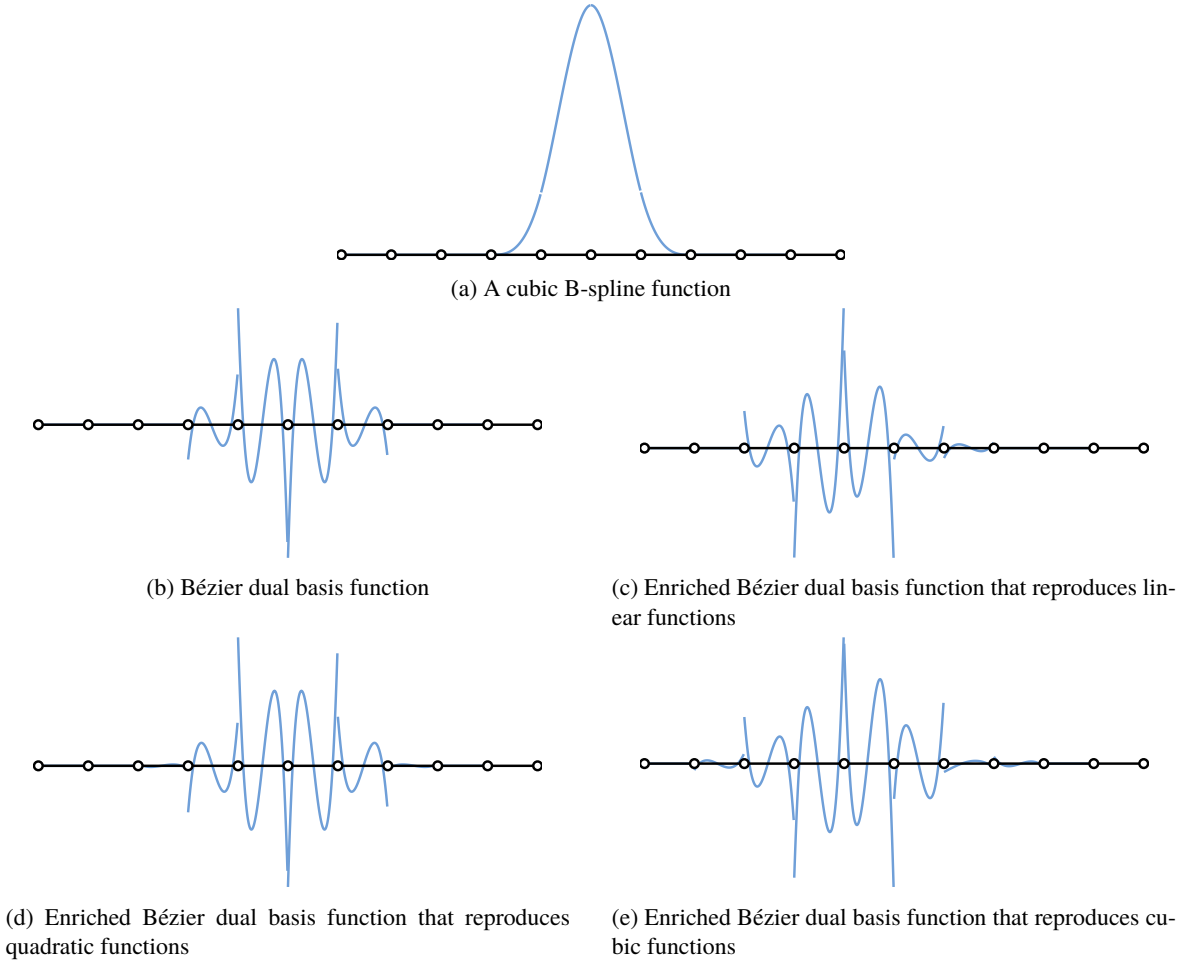(e) Enriched Bézier dual basis function that reproduces cubic functions

Figure 9: A cubic B-spline basis function and its corresponding enriched Bézier dual basis functions with different polynomial reproduction orders.

5.2 The dual mortar formulation

We introduce the dual mortar method in the context of the following abstract variational problem. Let $\mathcal{V}$ be a Hilbert space that satisfies homogeneous Dirichlet boundary conditions on $\partial\Omega$. For a given $f \in \mathcal{V}'$, find $u \in \mathcal{V}$ such that

$$a(u,v) = l(v) \qquad \forall v \in \mathcal{V}, \tag{64}$$

where $a(\cdot,\cdot)$ is a bilinear form representing an internal potential energy and $l(\cdot)$ is a linear form representing the external load.

In order to approximate the solution of the variational problem (64) on the decomposed domain $\Omega = \bigcup_{k=1}^{K} \Omega_k$, each subdomain is discretized with non-conforming NURBS patches. The discrete spaces satisfying the homogeneous Dirichlet boundary conditions are denoted by $\{\mathcal{X}_k\}_{k=1}^{K}$, where $\mathcal{X}_k$ is in $H^1(\Omega_k)$ for second-order problems and $H^2(\Omega_k)$ for fourth-order problems. However, the function space

$$\mathcal{X} := \left\{ v \in L^2(\Omega) \quad | \quad v|_{\Omega_k} \in \mathcal{X}_k, \quad l \in \{1,2,\ldots,K\} \right\} \tag{65}$$

is not compatible with the variational problem since functions in $\mathcal{X}$ are discontinuous across each intersection.

One solution to this problem is to modify the variational formulation (64) so that it becomes a saddle point problem: Find $(u,\lambda) \in \mathcal{X} \times \mathcal{M}$, such that

$$\begin{cases} a(u,v) + b(v,\lambda) = l(v) & \forall v \in \mathcal{X}, \\ b(u,\mu) = 0 & \forall \mu \in \mathcal{M}, \end{cases} \tag{66}$$
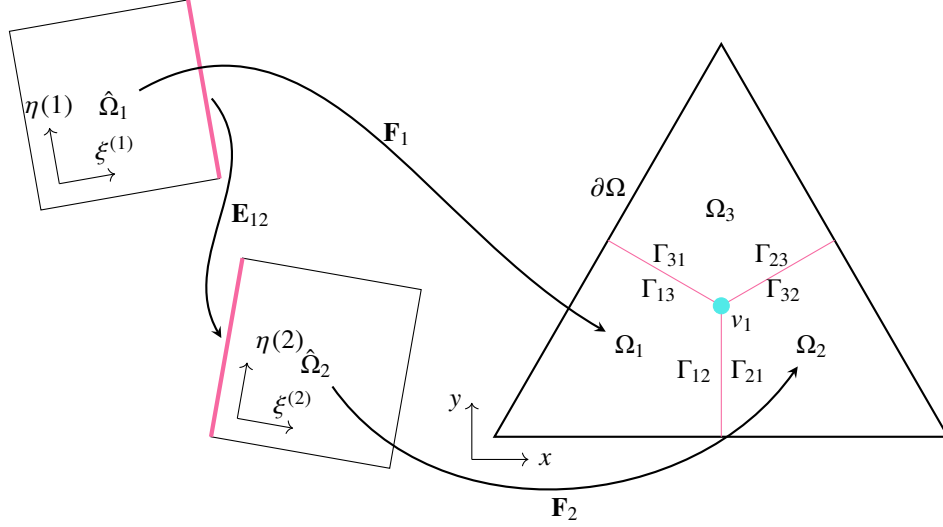
18

Figure 10: An example of a domain decomposition of a triangular domain. The patches are defined on different parametric domains and are connected via geometric mappings.

where $b(\cdot, \cdot)$, enforced by the Lagrange multiplier λ, is an abstract bilinear form describing the coupling constraints between slave and master patches and $\mathcal{M}$ is a Lagrange multiplier space defined on the skeleton $\mathbf{S}$. In order to recover the positive definite variational formulation (64), Bernardi et al. [7] introduced the following constrained space

$$\mathcal{V} := \{v \in \mathcal{X} \quad | \quad b(v, \mu) = 0, \quad \forall \mu \in \mathcal{M}\}. \tag{67}$$

Then, the saddle point problem (66) is equivalent to the minimization problem (64) on the function space $\mathcal{V}$. The advantage of using a dual basis with compact support to discretize the Lagrange multiplier space is that the basis functions of the discretized constrained space $\mathcal{V}^h$ are much easier to construct. In particular, all the basis functions of $\mathcal{V}^h$ have compact support. In general, this is not possible if the basis functions of $\mathcal{V}^h$ are constructed using a traditional Lagrange multiplier space or a globally constructed dual basis. In the latter case, the support of a dual basis function is the entire slave side of an intersection.

We can rewrite the discretized saddle point problem in matrix form:

$$\begin{bmatrix} \mathbf{K} & \mathbf{B}^T \\ \mathbf{B} & \mathbf{0} \end{bmatrix} \begin{bmatrix} \mathbf{U} \\ \mathbf{\Lambda} \end{bmatrix} = \begin{bmatrix} \mathbf{F} \\ \mathbf{0} \end{bmatrix}, \tag{68}$$

where $\mathbf{K}$ is the discretized stiffness matrix, $\mathbf{F}$ is the discretized external force vector, $\mathbf{B}$ is the discretized constraint matrix, and $\mathbf{U}$ is a nodal vector from the discretized displacement field $u^h \in \mathcal{X}^h$ and $\mathbf{\Lambda}$ is a nodal vector from the discretized Lagrange multiplier field $\lambda^h \in \mathcal{M}^h$. In vector form, the basis functions of $\mathcal{V}^h$ can be written as

$$\mathbf{N}^{\mathcal{V}^h} = \left[\mathbf{B}^\perp\right]^T \mathbf{N}^{\mathcal{X}^h}, \tag{69}$$

where $\mathbf{N}^{\mathcal{X}^h}$ are the basis functions of $\mathcal{X}^h$ in vector form. All column vectors of $\mathbf{B}^\perp$ are linearly independent and they span the null space of $\mathbf{B}$. We can further partition $\mathbf{U}$ as

$$\mathbf{U} = \begin{bmatrix} \mathbf{U}_s \\ \mathbf{U}_m \\ \mathbf{U}_{in} \end{bmatrix}, \tag{70}$$

where the slave nodal vector $\mathbf{U}_s$ consists of all degrees of freedom that will be eliminated after static condensation, the master nodal vector $\mathbf{U}_m$ consists of all degrees of freedom on the intersection that will not be eliminated after static condensation, and the inactive nodal vector $\mathbf{U}_{in}$ consists of all degrees of freedom that do not contribute to the

construction of $\mathbf{B}$. The constraint can then be rewritten as

$$\mathbf{B}\mathbf{U} = \begin{bmatrix} \mathbf{B}_s & \mathbf{B}_m & \mathbf{0} \end{bmatrix} \begin{bmatrix} \mathbf{U}_s \\ \mathbf{U}_m \\ \mathbf{U}_{in} \end{bmatrix} = \mathbf{0}. \tag{71}$$

If the Lagrange multiplier space is discretized with dual basis functions and the continuity constraint is dual compatible, $\mathbf{B}_s$ is the identity matrix, and the bandwidth of $\mathbf{B}_m$ depends on the support size of the dual basis functions. For a constraint matrix $\mathbf{B}$, constructed with dual basis functions with compact support, $\mathbf{B}_m$ is a sparse matrix with limited bandwidth, while global dual basis functions lead to a dense $\mathbf{B}_m$. For a $\mathbf{B}$ that takes the form (71) with $\mathbf{B}_s = \mathbf{I}$, the corresponding $\mathbf{B}^\perp$ can be obtained from

$$\mathbf{B}^\perp = \begin{bmatrix} -\mathbf{B}_m & \mathbf{0} \\ \hline \mathbf{I} \end{bmatrix}. \tag{72}$$

We then have the following linear system to solve

$$\mathbf{K}^{\text{mortar}}\mathbf{U}^{\text{mortar}} = \begin{bmatrix} \mathbf{B}^\perp \end{bmatrix}^T \mathbf{K}\mathbf{B}^\perp \mathbf{U}^{\text{mortar}} = \begin{bmatrix} \mathbf{B}^\perp \end{bmatrix}^T \mathbf{F} \tag{73}$$

where the relationship between the mortar displacement nodal vector $\mathbf{U}^{\text{mortar}}$ and $\mathbf{U}$ is given by

$$\mathbf{U} = \mathbf{B}^\perp \mathbf{U}^{\text{mortar}}. \tag{74}$$

With a sparse $\mathbf{B}^\perp$ obtained from dual basis functions with compact support, the stiffness matrix of the mortar formulation $\mathbf{K}^{\text{mortar}}$ will be sparse.

5.3 Vertex modification

For a multi-patch decomposition, at least three patches will meet at a common interior vertex and several interfaces can share this vertex as a common endpoint. If we discretize the Lagrange multiplier space with a space of the same dimension as the univariate space formed by taking the trace of the slave space along the interface, we obtain too many constraints. In this case, nodes in the neighborhood of a vertex may serve as both slave and master nodes and the matrix $\mathbf{B}^\perp$ cannot be formed elegantly using (72). Hence, modifications to the Lagrange multiplier space in the neighborhood of vertices are needed to relax the overly constrained linear system. Note that these modifications are also commonly called cross point modifications [13, 69].

In general, these vertex modifications can be achieved by reducing the dimension of the Lagrange multiplier space. For second order problems, a Lagrange multiplier space of codimension (the difference between the dimension of a certain space and the dimension of its subspace) 2 of the trace space of the slave side is sufficient to remove redundant constraints. For fourth order problems, a Lagrange multiplier space of codimension 4 of the trace space of the slave side is preferred. To construct an enriched dual basis of codimension $2c$, we remove the first c and the last c vectors in $\{\mathbf{A}_i\}_{i=0}^{n_N-1}$, leaving $\{\mathbf{A}_i\}_{i=c}^{n_N-1-c}$ a $n_N - 2c$-dimensional vector space. The orthonormal vector basis of the null space of $\text{span}\{\mathbf{A}_i\}_{i=c}^{n_N-1-c}$ can be written as $\{\mathbf{A}_i^\perp\}_{i=0}^{n_B-n_N-1} \bigcup \{\bar{\mathbf{A}}_i\}_{i=0}^{c-1} \bigcup \{\bar{\mathbf{A}}_i\}_{i=n_N-c}^{n_N-1}$. Now, we can construct $\mathbf{W}^{\text{ini}}$ from $\{\mathbf{A}_i\}_{i=c}^{n_N-1-c}$ via (41) and assemble $\mathbf{W}^{\text{mod}}$ from $\{\mathbf{A}_i^\perp\}_{i=0}^{n_B-n_N-1} \bigcup \{\bar{\mathbf{A}}_i\}_{i=0}^{c-1} \bigcup \{\bar{\mathbf{A}}_i\}_{i=n_N-c}^{n_N-1}$ with Algorithm 4. The resulting dual basis has $2c$ fewer dimensions than the original basis and satisfies global idempotence.

6 Dual mortaring for second-order problems

To approximate the solution of second-order variational problem, we use B-spline basis functions $\{N_i\}_{i \in \cup_{k=1}^K I_k}$ to discretize each subdomain, where I_k is the index set for domain Ω_k. An appropriate indexing is chosen so that there is no overlap among the index sets $\{I_k\}_{k=1}^K$. The discretized test and weighting functions are

$$u^h = \sum_{i \in \cup_{k=1}^K I_k} U_i N_i, \quad v^h = \sum_{i \in \cup_{k=1}^K I_k} V_i N_i. \tag{75}$$
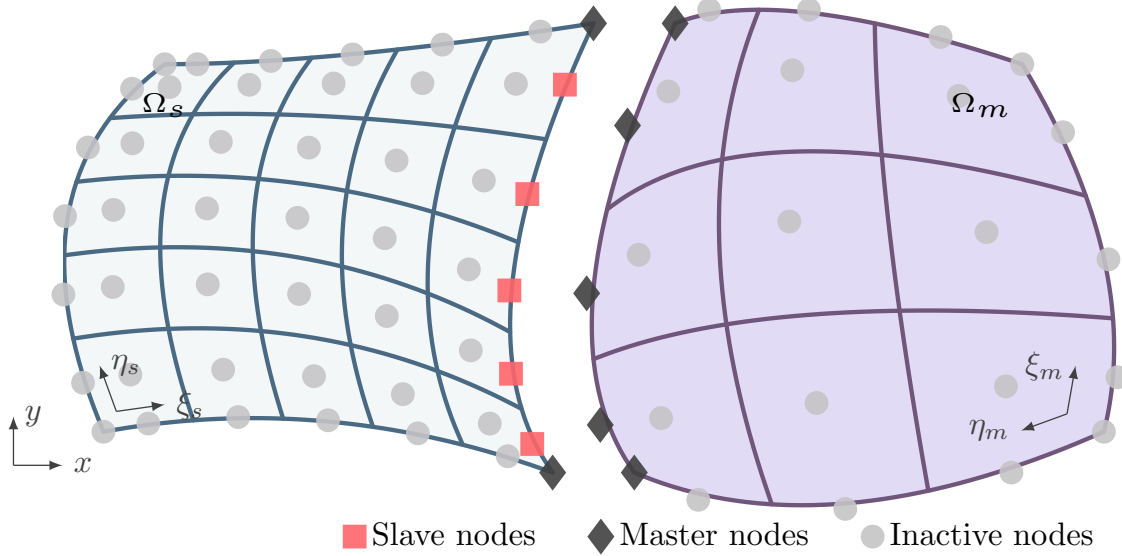
Figure 11: The classification of nodes along the interface for a second-order problem over a two-patch domain.

Due to the existence of a first-order weak derivative in the weak form of second-order problems, the constrained space $\mathcal{V}^h$ should weakly satisfy a C^0 continuity constraint across each interface $\Gamma \in \mathcal{S}$. Hence, the constrained space $\mathcal{V}^h$ for second-order problems is given by

$$\mathcal{V}^h := \left\{ u^h \in \mathcal{X}^h \mid b_0(u^h, \mu^h) = 0, \quad \forall \mu^h \in \cup_{\Gamma \in \mathbf{S}} \mathcal{M}^h(\Gamma) \right\}, \tag{76}$$

where

$$b_0(u^h, \mu^h) = \sum_{\Gamma \in \mathbf{S}} \int_\Gamma \mu^h \left[u^h \right]_\Gamma d\Gamma, \tag{77}$$

and $[\cdot]_\Gamma := \cdot|_{\Omega_s(\Gamma)} - \cdot|_{\Omega_m(\Gamma)}$ denotes a jump from master to slave. For each intersection $\Gamma \in \mathbf{S}$, the discretized Lagrange multiplier and its variation in $\mathcal{M}^h(\Gamma)$ can be written as

$$\lambda^h = \sum_{i=0}^{n_s(\Gamma)-3} \Lambda_i \hat{N}_i, \quad \mu^h = \sum_{i=0}^{n_s(\Gamma)-3} \delta \Lambda_i \hat{N}_i \tag{78}$$

where $\hat{N}_i$ and $n_s(\Gamma)$ are dual basis functions and the dimension of the discretized trace space along the slave side of Γ, respectively. Hence, $\mathcal{M}^h(\Gamma)$ is two dimensions less than the trace space along the slave side of Γ. As a result, in addition to the interface nodes along the master side of the interface, the first and the last interface nodes along the slave side also serve as master nodes. An example of the node classification for a two-patch domain is shown in Figure 11.

The structure of the discretized constraint matrix $\mathbf{B}$ depends on the index sets $\{I_k\}_{k=1}^K$ and the ordering of the Lagrange multiplier basis functions. We introduce a column-wise permutation matrix $\mathbf{P}_c$ as

$$\begin{bmatrix} \mathbf{I}_1 \\ \mathbf{I}_2 \\ \vdots \\ \mathbf{I}_K \end{bmatrix} = \mathbf{P}_c \begin{bmatrix} \mathbf{I}_s \\ \mathbf{I}_m \\ \mathbf{I}_{in} \end{bmatrix}, \tag{79}$$

where $\mathbf{I}_s$ is the vector form of all indices of $\mathbf{U}_s$, $\mathbf{I}_m$ is the vector form of all indices of $\mathbf{U}_m$, $\mathbf{I}_{in}$ is the vector form of all indices of $\mathbf{U}_{in}$ and $\mathbf{I}_i$ is the vector form of the index set I_i. Then there exists a row-wise permutation matrix $\mathbf{P}_r$ such that the permuted constraint matrix $\mathbf{B}_p = \mathbf{P}_r \mathbf{B} \mathbf{P}_c$ shares the same structure as Equation (71). We may construct $\mathbf{B}_p^\perp$ by Equation (72). The vector basis of the null space of $\mathbf{B}$ can now be obtained from

$$\mathbf{B}^\perp = \mathbf{P}_c \mathbf{B}_p^\perp. \tag{80}$$

The sparsity patterns for the stiffness matrices corresponding to the two-patch Poisson problem using the global dual basis, the Bézier dual basis and the enriched Bézier dual basis are shown in Figure 12. Note that the matrix constructed using the global dual basis is denser than the matrix constructed using the Bézier dual basis and the enriched Bézier dual basis achieves a balance between sparsity and optimal approximation.
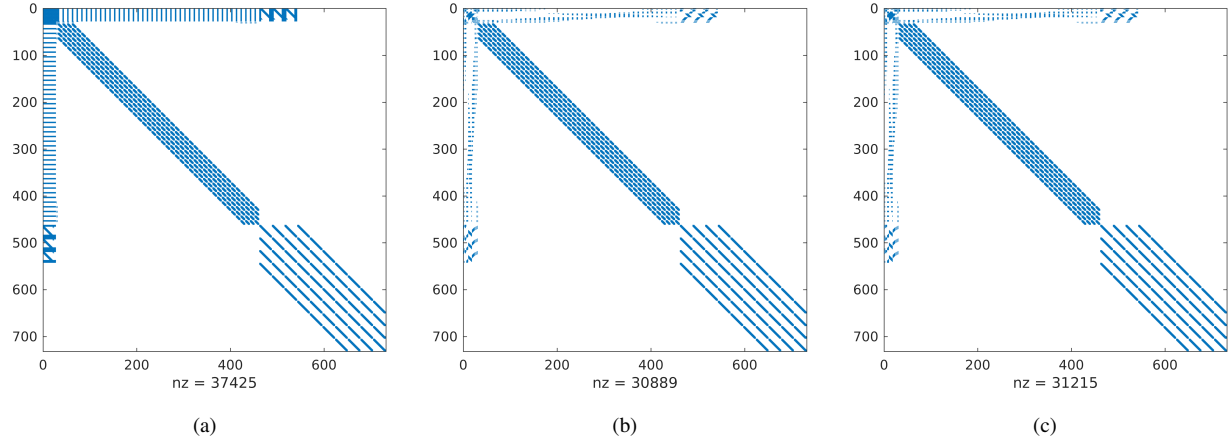

(a)   (b)   (c)

Figure 12: Stiffness matrix sparsity patterns for the coupled linear system using (a) global dual basis, (b) Bézier dual basis, and (c) enriched Bézier dual basis for a Poisson problem. The stiffness matrices are computed from the two-patch domain in Figure 11 after three levels of refinements.

7 Dual mortaring for fourth-order problems

Due to the existence of a second-order weak derivative in the weak form of fourth-order problems, the constrained space $\mathcal{V}^h$ should weakly satisfy a C^1 continuity constraint across each interface $\Gamma \in \mathbf{S}$. We now develop a set of constraints to impose C^1 continuity across patch boundaries under the dual mortar framework.
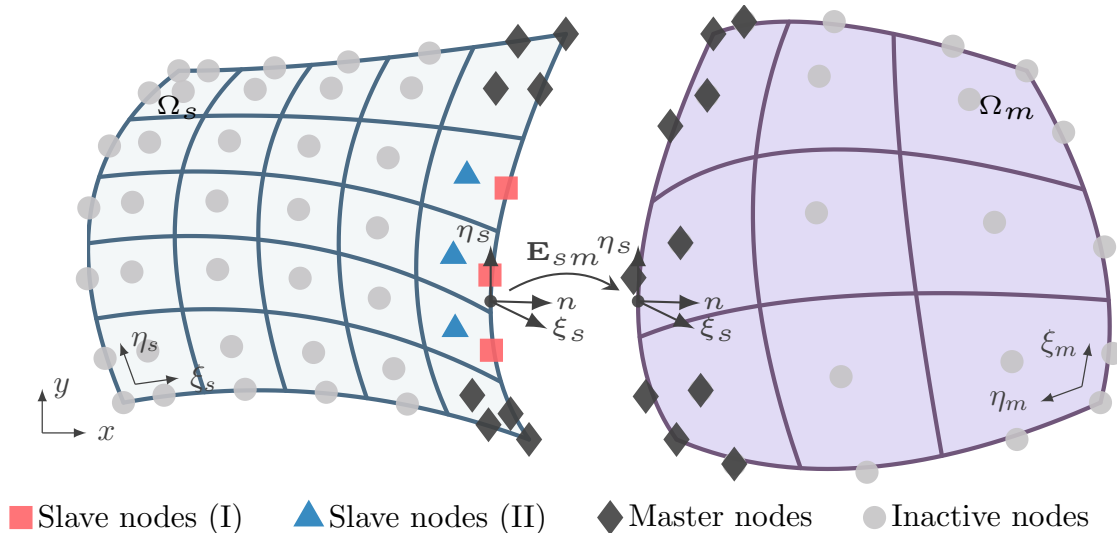
Figure 13: The classification of nodes along an interface for 4th-order problems.

To illustrate our method, we consider the construction of C^1 constraints for the two-patch domain shown in Figure 13. For a function $u \in C^1(\Omega_s \cup \Omega_m)$ with $u|_{\Omega_s} \in C^1(\Omega_s)$, $u|_{\Omega_m} \in C^1(\Omega_m)$ the following two constraints are required across

the intersection Γ:

$$[u]_\Gamma = 0, \tag{81a}$$

$$\left[\frac{\partial u}{\partial \mathbf{n}}\right]_\Gamma = 0, \quad \text{with } \mathbf{n} = \mathbf{n}_s = -\mathbf{n}_m, \tag{81b}$$

where $\mathbf{n}_k$ is the outward normal direction of $\partial \Omega_k$. The continuity constraint (81a) can naturally be incorporated into the framework of the dual mortar formulation. The smoothness constraint (81b), however, can not be directly imposed. First, the existence of a dual basis for $\frac{\partial N_i}{\partial \mathbf{n}}|_\Gamma$ is doubtful. Even if these dual basis functions do exist, since they are biorthogonal to the normal derivative of the basis functions, their formulation will depend on the parameterization of Γ and the geometric information of Ω_s. This complex geometric dependence would destroy the simplicity of the dual basis formulation. To overcome this issue, we instead propose a smoothness constraint involving parametric derivatives only.

Lemma 4. *Given two differentiable bijective geometric mappings* $\mathbf{F}_s : \hat{\Omega}_s \to \Omega_s$ *and* $\mathbf{F}_m : \hat{\Omega}_m \to \Omega_m$, *a* C^0-*continuous function u is* C^1-*continuous in the physical domain if and only if*

$$\left[\frac{\partial u}{\partial \xi_s}\right]_\Gamma = 0 \quad \text{and} \quad \left[\frac{\partial u}{\partial \eta_s}\right]_\Gamma = 0. \tag{82}$$

Proof. It suffices to consider two neighboring patches as shown in Figure 13. In this configuration, if u is a C^0-continuous function then $[\frac{\partial u}{\partial \eta_s}]_\Gamma = 0$. If u is also C^1-continuous, we have

$$0 = \left[\frac{\partial u}{\partial \mathbf{n}}\right]_\Gamma = \left[\frac{\partial u}{\partial \xi_s}\right]_\Gamma \frac{\partial \xi_s}{\partial \mathbf{n}} + \left[\frac{\partial u}{\partial \eta_s}\right]_\Gamma \frac{\partial \eta_s}{\partial \mathbf{n}} \implies \left[\frac{\partial u}{\partial \xi_s}\right]_\Gamma \frac{\partial \xi_s}{\partial \mathbf{n}} = 0 \tag{83}$$

The fact that $\mathbf{F}_s$ is bijective and $\frac{\partial \eta_s}{\partial \mathbf{n}} = 0$ indicates $\frac{\partial \xi_s}{\partial \mathbf{n}} \neq 0$. Hence, $\left[\frac{\partial u}{\partial \xi_s}\right]_\Gamma = 0$. On the other hand,

$$\begin{cases} \left[\frac{\partial u}{\partial \xi_s}\right]_\Gamma = 0 \\ \left[\frac{\partial u}{\partial \eta_s}\right]_\Gamma = 0 \end{cases} \implies \left[\frac{\partial u}{\partial \mathbf{n}}\right]_\Gamma = \left[\frac{\partial u}{\partial \xi_s}\right]_\Gamma \frac{\partial \xi_s}{\partial \mathbf{n}} + \left[\frac{\partial u}{\partial \eta_s}\right]_\Gamma \frac{\partial \eta_s}{\partial \mathbf{n}} = 0 \tag{84}$$

This concludes the proof. $\qquad \square$

Hence, the constraints in (82) are equivalent to constraint (81b). On an intersection that is parallel to the η_s direction in the parametric domain, the constraint $\left[\frac{\partial u}{\partial \xi_s}\right]_\Gamma = 0$ is utilized while on an intersection that is parallel to the ξ_s direction in the parametric domain, the constraint $\left[\frac{\partial u}{\partial \eta_s}\right]_\Gamma = 0$ is utilized.

Remark 2. *In order to demonstrate the advantages of the constraints in (82), we consider the following intergral:*

$$\int_\Gamma \frac{\partial N_a(\xi_s, \eta_s)}{\partial \xi_s} \hat{N}_j(\eta_s) d\Gamma = \int_\Gamma \frac{\partial N_{n_{\xi_s}-2}(1) N_i(\eta_s)}{\partial \xi_s} \hat{N}_j(\eta_s) d\Gamma \qquad i, j \in \{0, 1, \dots, n_{\eta_s} - 1\} \tag{85}$$
$$= \frac{\partial N_{n_{\xi_s}-2}(1)}{\partial \xi_s} \int_\Gamma N_i(\eta_s) \hat{N}_j(\eta_s) d\Gamma$$

where n_{ξ_s} *and* n_{η_s} *are the number of nodes in the* ξ_s *and* η_s *directions of the slave patch, respectively. This integral is one term that is involved in the discretization of the constraint (81b) and is constructed from a Lagrange multiplier basis function* $\hat{N}_j(\eta_s)$ *and an activated basis function of the slave patch* $N_a(\xi_s, \eta_s)$ *that is one column away from the intersection (denoted by the blue triangles in Figure 13). Due to the tensor product structure of multivariate spline basis functions, the derivative in one direction (* ξ_s *for this case) will not influence the contributions coming from other directions. Hence, the dual basis function of an activated basis function in the constraint* $\left[\frac{\partial u}{\partial \xi_s}\right]_\Gamma = 0$ *can be constructed by the dual basis function of its* η_s *component divided by* $\frac{\partial N_{n_{\xi_s}-2}(1)}{\partial \xi_s}$.

The only issue now is how to evaluate the derivative of u_m w.r.t. ξ_s or η_s directions. This can be done by considering the following chain rule

$$\begin{bmatrix} \frac{\partial u_m}{\partial \xi_s} \\ \frac{\partial u_m}{\partial \eta_s} \end{bmatrix} = \begin{bmatrix} \frac{\partial \xi_m}{\partial \xi_s} & \frac{\partial \xi_m}{\partial \eta_s} \\ \frac{\partial \eta_m}{\partial \xi_s} & \frac{\partial \eta_m}{\partial \eta_s} \end{bmatrix}^T \cdot \begin{bmatrix} \frac{\partial u_m}{\partial \xi_m} \\ \frac{\partial u_m}{\partial \eta_m} \end{bmatrix} = \nabla \mathbf{E}_{sm}^T \cdot \begin{bmatrix} \frac{\partial u_m}{\partial \xi_m} \\ \frac{\partial u_m}{\partial \eta_m} \end{bmatrix}. \tag{86}$$

Hence, two Lagrange multipliers are needed to apply both a C^0 continuity constraint and a C^1 continuity constraint. The constrained space $\mathcal{V}^h$ for fourth-order problems is given by

$$\mathcal{V}^h := \left\{ v \in \mathcal{X}^h \; \middle| \; \begin{cases} b_0(u^h, \mu_0^h) = 0, & \forall \mu_0^h \in \cup_{\Gamma \in \mathbf{S}} \mathcal{M}_0^h(\Gamma) \\ b_1(u^h, \mu_1^h) = 0, & \forall \mu_1^h \in \cup_{\Gamma \in \mathbf{S}} \mathcal{M}_1^h(\Gamma) \end{cases} \right\}, \tag{87}$$

where

$$b_1(u^h, \mu_1^h) = \sum_{\Gamma \in \mathbf{S}} \int_\Gamma \mu_1^h \left[\frac{\partial u^h}{\partial \xi_s} \right]_\Gamma d\Gamma = 0 \text{ if } \Gamma \parallel \eta_s, \text{ or } b_1(u^h, \mu_1^h) = \sum_{\Gamma \in \mathbf{S}} \int_\Gamma \mu_1^h \left[\frac{\partial u^h}{\partial \eta_s} \right]_\Gamma d\Gamma = 0 \text{ if } \Gamma \parallel \xi_s. \tag{88}$$

Depending on the orientation of the intersection, the discretized Lagrange multipliers and their variations in $\mathcal{M}_0^h(\Gamma)$ and $\mathcal{M}_1^h(\Gamma)$ can be written as:

- for the intersection $\xi_s = 0$,

$$\lambda_0^h = \sum_{i=0}^{n_s(\Gamma)-5} \Lambda_i^0 \hat{N}_i, \quad \mu_0^h = \sum_{i=0}^{n_s(\Gamma)-5} \delta\Lambda_i^0 \hat{N}_i$$

$$\lambda_1^h = \sum_{i=0}^{n_s(\Gamma)-5} \Lambda_i^1 \frac{\hat{N}_i}{c}, \quad \mu_1^h = \sum_{i=0}^{n_s(\Gamma)-5} \delta\Lambda_i^1 \frac{\hat{N}_i}{c}, \quad c = \left. \frac{\partial N_1^s(\xi_s)}{\partial \xi_s} \right|_{\xi_s=0}, \tag{89}$$

- for the intersection $\xi_s = 1$,

$$\lambda_0^h = \sum_{i=0}^{n_s(\Gamma)-5} \Lambda_i^0 \hat{N}_i, \quad \mu_0^h = \sum_{i=0}^{n_s(\Gamma)-5} \delta\Lambda_i^0 \hat{N}_i$$

$$\lambda_1^h = \sum_{i=0}^{n_s(\Gamma)-5} \Lambda_i^1 \frac{\hat{N}_i}{c}, \quad \mu_1^h = \sum_{i=0}^{n_s(\Gamma)-5} \delta\Lambda_i^1 \frac{\hat{N}_i}{c}, \quad c = \left. \frac{\partial N_{n_{\xi_s}-2}^s(\xi_s)}{\partial \xi_s} \right|_{\xi_s=1}, \tag{90}$$

- for the intersection $\eta_s = 0$,

$$\lambda_0^h = \sum_{i=0}^{n_s(\Gamma)-5} \Lambda_i^0 \hat{N}_i, \quad \mu_0^h = \sum_{i=0}^{n_s(\Gamma)-5} \delta\Lambda_i^0 \hat{N}_i$$

$$\lambda_1^h = \sum_{i=0}^{n_s(\Gamma)-5} \Lambda_i^1 \frac{\hat{N}_i}{c}, \quad \mu_1^h = \sum_{i=0}^{n_s(\Gamma)-5} \delta\Lambda_i^1 \frac{\hat{N}_i}{c}, \quad c = \left. \frac{\partial N_1^s(\eta_s)}{\partial \eta_s} \right|_{\eta_s=0}, \tag{91}$$

- for the intersection $\eta_s = 1$,

$$\lambda_0^h = \sum_{i=0}^{n_s(\Gamma)-5} \Lambda_i^0 \hat{N}_i, \quad \mu_0^h = \sum_{i=0}^{n_s(\Gamma)-5} \delta\Lambda_i^0 \hat{N}_i$$

$$\lambda_1^h = \sum_{i=0}^{n_s(\Gamma)-5} \Lambda_i^1 \frac{\hat{N}_i}{c}, \quad \mu_1^h = \sum_{i=0}^{n_s(\Gamma)-5} \delta\Lambda_i^1 \frac{\hat{N}_i}{c}, \quad c = \left. \frac{\partial N_{n_{\eta_s}-2}^s(\eta_s)}{\partial \eta_s} \right|_{\eta_s=1}. \tag{92}$$

Note that both $\mathcal{M}_0^h(\Gamma)$ and $\mathcal{M}_1^h(\Gamma)$ are four dimensions less than the trace space along the slave side of Γ. Hence, four nodes in the neighborhood of each vertex of Ω_s are classified as master nodes (see Figure 13).

Due to the presence of two constraints in the definition of $\mathcal{V}^h$, the discretized constraint matrix can be written as

$$\mathbf{B} = \begin{bmatrix} \mathbf{B}_0 \\ \mathbf{B}_1 \end{bmatrix}, \tag{93}$$

where $\mathbf{B}_0$ and $\mathbf{B}_1$ correspond to the discretized C^0 and C^1 constraints. In order to recover the form (71), we subdivide the slave nodes into two types, as shown in Figure 13:

I The second closest column of slave basis functions to each intersection $\Gamma \in \mathbf{S}$, whose indices are denoted by the index set I_s^I. (denoted by blue triangles)

II The column of slave basis functions on the intersection $\Gamma \in \mathbf{S}$, whose indices are denoted by the index set I_s^II. (denoted by red squares)

Similar to Section 6, we define a column-wise permutation matrix $\mathbf{P}_\mathrm{c}$ as

$$
\begin{bmatrix} \mathbf{I}_1 \\ \mathbf{I}_2 \\ \vdots \\ \mathbf{I}_K \end{bmatrix} = \mathbf{P}_\mathrm{c} \begin{bmatrix} \mathbf{I}_\mathrm{s}^\mathrm{I} \\ \mathbf{I}_\mathrm{s}^\mathrm{II} \\ \mathbf{I}_\mathrm{m} \\ \mathbf{I}_\mathrm{in} \end{bmatrix},
\tag{94}
$$

Then, there exist a row-wise permutation matrix $\mathbf{P}_\mathrm{r}$ such that

$$
\mathbf{B}_\mathrm{p} = \mathbf{P}_\mathrm{r} \mathbf{B} \mathbf{P}_\mathrm{c} = \begin{bmatrix} \mathbf{B}_1^1 & \mathbf{B}_1^2 & \mathbf{B}_1^3 & \mathbf{0} \\ \mathbf{0} & \mathbf{B}_2^2 & \mathbf{B}_2^3 & \mathbf{0} \end{bmatrix},
\tag{95}
$$

where $\mathbf{B}_1^1$ is the contribution of the slave nodes (I) in the discretization of the C^1 continuity constraint and $\mathbf{B}_2^2$ is the contribution of slave nodes (II) in the discretization of the C^0 continuity constraint. Under the row-wise permutation matrix $\mathbf{P}_\mathrm{r}$, $\mathbf{B}_1^1$ and $\mathbf{B}_2^2$ become identity submatrices. Under a rank-preserving transformation $\mathbf{T}$ we can eliminate the submatrix $\mathbf{B}_1^2$ such that

$$
\mathbf{T}\mathbf{B}_\mathrm{p} = \begin{bmatrix} \mathbf{I} & \Big| & \mathbf{B}_1^3 - \mathbf{B}_1^2 \mathbf{B}_2^3 & \mathbf{0} \\ & \Big| & \mathbf{B}_2^3 & \mathbf{0} \end{bmatrix}.
\tag{96}
$$

We may now take

$$
\mathbf{B}_\mathrm{p}^\perp = \begin{bmatrix} \mathbf{B}_1^2 \mathbf{B}_2^3 - \mathbf{B}_1^3 & \mathbf{0} \\ -\mathbf{B}_2^3 & \mathbf{0} \\ \hdashline \mathbf{I} & \end{bmatrix}.
\tag{97}
$$

The vector basis of the null space of $\mathbf{B}$ can now be obtained from

$$
\mathbf{B}^\perp = \mathbf{P}_\mathrm{c} \mathbf{B}_\mathrm{p}^\perp.
\tag{98}
$$

Examples of basis functions, represented by vectors of $\mathbf{B}^\perp$, are shown in Figure 14.
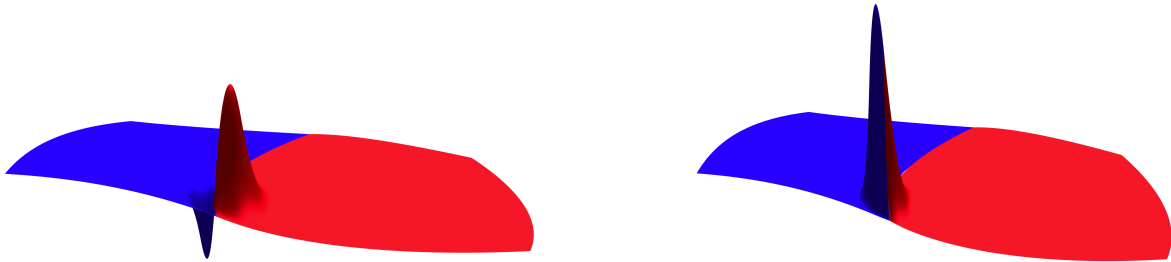

Figure 14: Two exemplary basis functions in the constrained space $\mathcal{V}^h$ for fourth-order problems.

The sparsity patterns for the stiffness matrices corresponding to the two-patch biharmonic problem using the global dual basis, the Bézier dual basis and the enriched Bézier dual basis are shown in Figure 15. The sparsity patterns for biharmonic problem are similar to that of the Poisson problem for all three types of dual basis functions.

8 Numerical examples

In this section, we investigate the performance of the enriched dual basis for several challenging second- and fourth-order benchmarks. Results obtained from the enriched Bézier dual basis are denoted by Enrich-Q_i. The performance
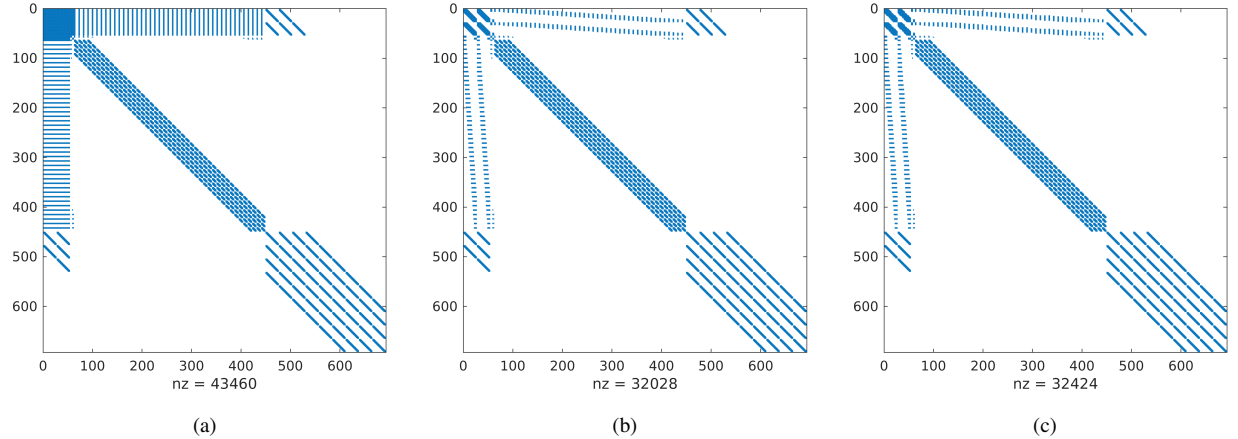
Figure 15: Stiffness matrix sparsity patterns for the coupled linear system using (a) global dual basis, (b) Bézier dual basis, and (c) enriched Bézier dual basis for the biharmonic problem. The stiffness matrices are computed from the two-patch domain in Figure 13 after three levels of refinements.

of the enriched dual basis is compared with the global dual basis (L^2-Q_i) and the Bézier dual basis (Bézier-Q_i). For all second order problems, the polynomial reproduction degree q is set to $p-1$ for the pth-order enriched dual basis. For all fourth-order problems, the polynomial reproduction degree q is set to $p-2$ for the pth-order enriched dual basis. These choices of degrees ensure the sparsest possible stiffness matrix while also maintaining optimality. The enriched dual bases are constructed with Algorithm 4.

In the context of second-order problems, we solve two benchmarks. The first benchmark is a Poisson problem over a four-patch square domain, where the intersections are all parameterized differently. In the second benchmark, we model an infinite plate with a hole using four non-conforming NURBS patches.

In the context of fourth-order problems, we solve three benchmarks. The first benchmark is a biharmonic problem over a five-patch square domain. A simply supported square Kirchhoff-Love plate is the second benchmark. In the last benchmark we consider the Cahn-Hilliard equation.

All numerical problems are solved using the Eigen library [30]. A conjugate gradient solver is used for all problems except in the case of the Cahn-Hilliard problem where the BiCGSTAB solver is used to handle the asymmetric consistent tangent matrix.

8.1 The Poisson problem

We start by solving the Poisson equation $-\Delta u = f$ over the domain $[0,1] \times [0,1]$. The domain is decomposed into four patches as shown in Figure 16a. A manufactured solution is given as

$$u(x, y) = \sin(2\pi x)\sin(2\pi y). \tag{99}$$

This manufactured solution satisfies the homogeneous Dirichlet boundary condition ($u = 0$) and is shown in Figure 16b.

Convergence plots in both the L^2 and H^1 norms are shown in Figure 17. We achieve optimal convergence for the enriched Bézier dual basis for all tested polynomial degrees ($p = 2, 3, \ldots, 5$) in both norms. For $p = 2, 3$, the error in the enriched dual basis is close to that of the global dual basis, whereas uniform shifts are observed for $p = 4, 5$. We speculate that the cause of these vertical shifts in the convergence curves is due to the non-matching parameterizations along each intersection. Since the enriched Bézier dual basis functions have a larger support size, the size of a corresponding extension element $\hat{\Omega}_e$ for the enriched dual basis will be significantly larger than that of the standard B-spline basis. As a result, the local approximation error of the enriched dual basis will be larger than that of the standard B-spline basis. The higher degree non-matching parameterizations seem to aggravate this error. However, regardless of the slight shift, the optimal convergence rates have been observed in both measures. The Bézier dual basis, as expected, demonstrates sub-optimal convergence in both the L^2 and H^1 norms for $p = 3, 4, 5$. In addition, in the asymptotic regime, the error increases as the polynomial degree is increased.

(a) A four-patch mesh where all intersections have both mis-matched parameterizations and non-conforming meshes.
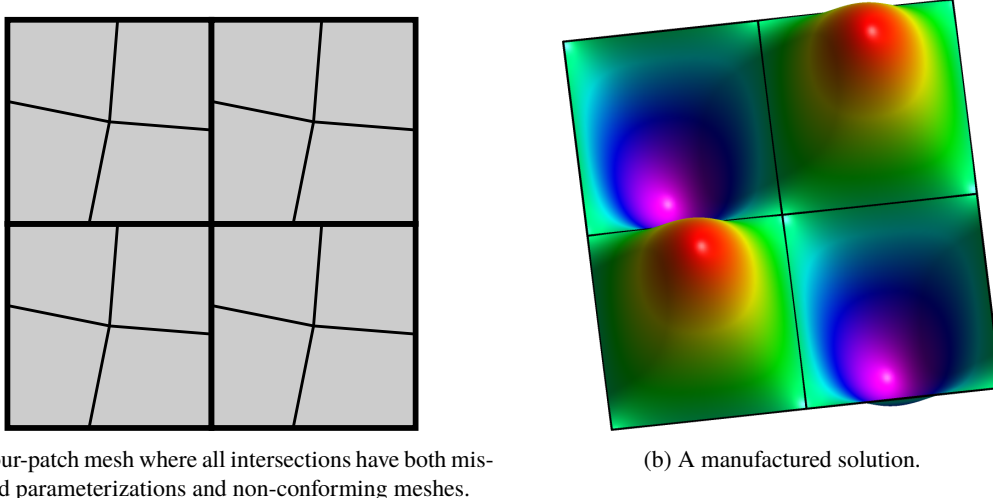

(b) A manufactured solution.

Figure 16: The multi-patch mesh of the domain $\Omega = [0,1] \times [0,1]$ and the manufactured solution that satisfies $u = 0$ on $\partial\Omega$, which are utilized for the problem described in Section 8.1.

Error plots for the cubic mesh after three global uniform refinements are shown in Figure 18. The plot of the error in the solution computed with the enriched Bézier dual basis is similar to that computed with the global dual basis, except for small spikes in the neighborhood of vertices. On the other hand, a significant amount of oscillatory error can be observed for the Bézier dual basis along each intersection. Notice that the error in the interior domain is similar in all cases.

8.2 Linear elasticity – infinite plate with a hole

We next consider a linear elasticity problem. The problem setup and multi-patch domain are shown in Figure 19. The traction along the outer edge is set to the exact solution

$$
\begin{aligned}
\sigma_{rr}(r,\theta) &= \frac{T_x}{2}(1 - \frac{R_1^2}{r^2}) + \frac{T_x}{2}(1 - 4\frac{R_1^2}{r^2} + 3\frac{R_1^4}{r^4})\cos(2\theta), \\
\sigma_{\theta\theta}(r,\theta) &= \frac{T_x}{2}(1 + \frac{R_1^2}{r^2}) - \frac{T_x}{2}(1 + 3\frac{R_1^4}{r^4})\cos(2\theta), \\
\sigma_{r\theta}(r,\theta) &= -\frac{T_x}{2}(1 + 2\frac{R_1^2}{r^2} - 3\frac{R_1^4}{r^4})\sin(2\theta).
\end{aligned}
\tag{100}
$$

The relative error of the displacement $\mathbf{u}$ are measured in both the L^2 norm and energy semi-norm

$$
\|\mathbf{u} - \mathbf{u}^h\|_E := \sum_k \int_{\Omega_k} \frac{1}{2}\sigma(\mathbf{u} - \mathbf{u}^h) : \epsilon(\mathbf{u} - \mathbf{u}^h) d\Omega.
\tag{101}
$$

Convergence plots for both norms are shown in Figure 20. Similar to the scalar Poisson problem, both the enriched Bézier and global dual basis converge optimally for all polynomial degrees in both norms. In addition, due to the absence of non-matching parameterizations along each intersection, the convergence plots of the enriched Bézier dual basis are all identical to that of the global dual basis. The convergence plots of the Bézier dual basis are again sub-optimal.

Error plots for $p = 3$ after three uniform global mesh refinements are shown in Figure 21. The error plots for both the enriched and global dual basis are the same. The error in the Bézier dual basis, however, is highly oscillatory along each intersection. Again, the in-domain errors are similar for all methods which confirms that the main contribution to the sub-optimal behavior is the consistency error.
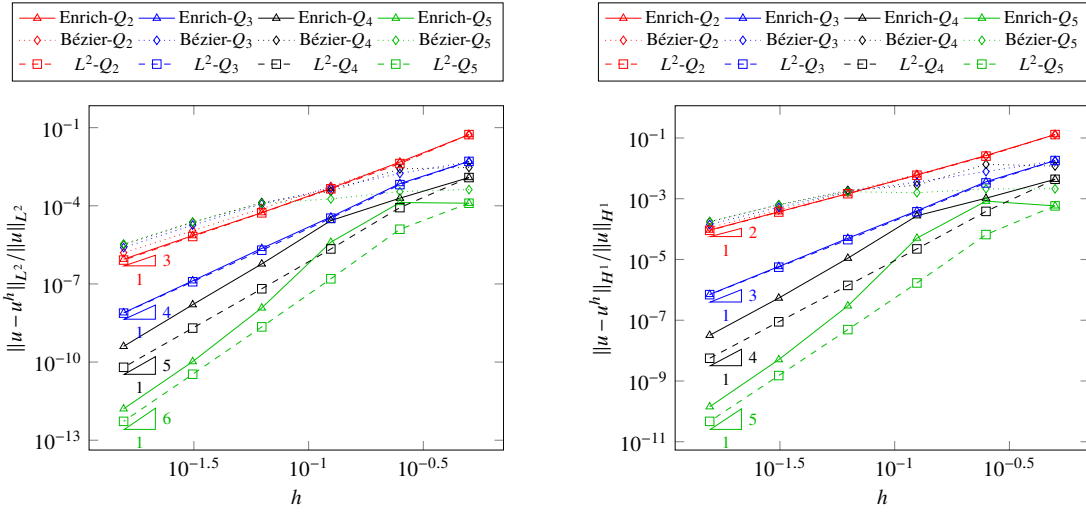
Figure 17: Convergence plots for the problem described in Section 8.1. On the left, error measured in the L^2 norm. On the right, error measured in the H^1 norm.
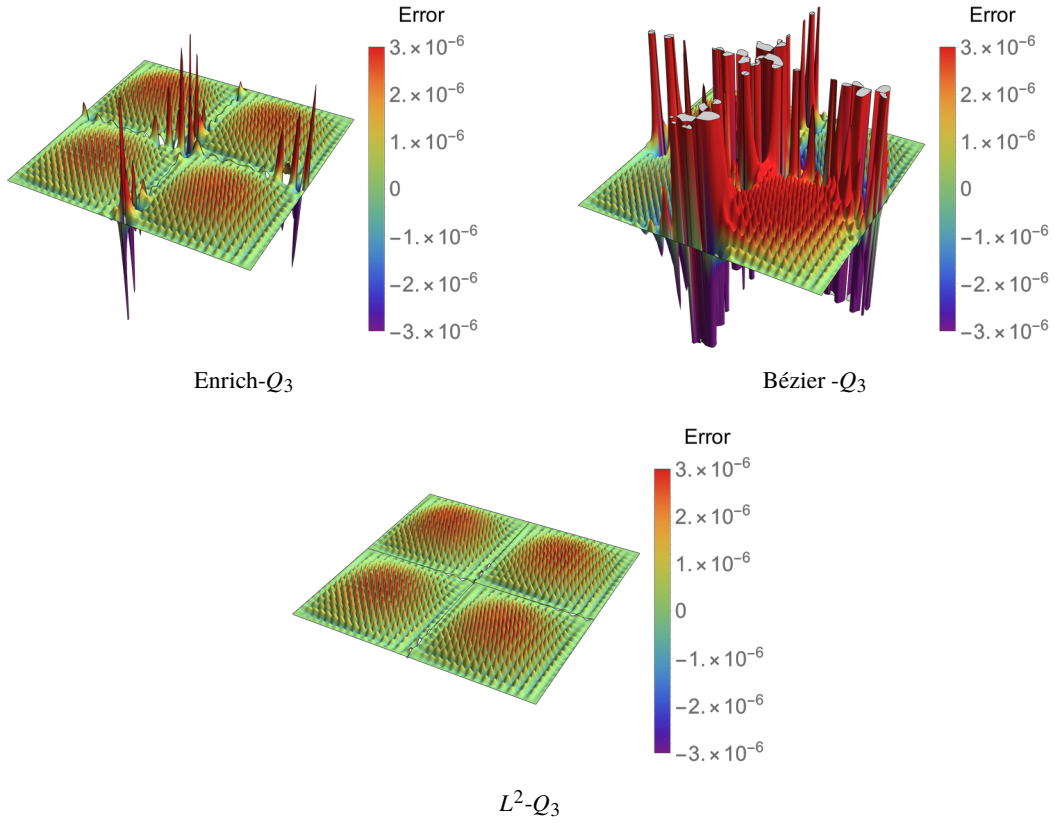

Figure 18: Error plots for the Poisson problem on a four-patch domain ($p = 3$, three uniform mesh refinements).
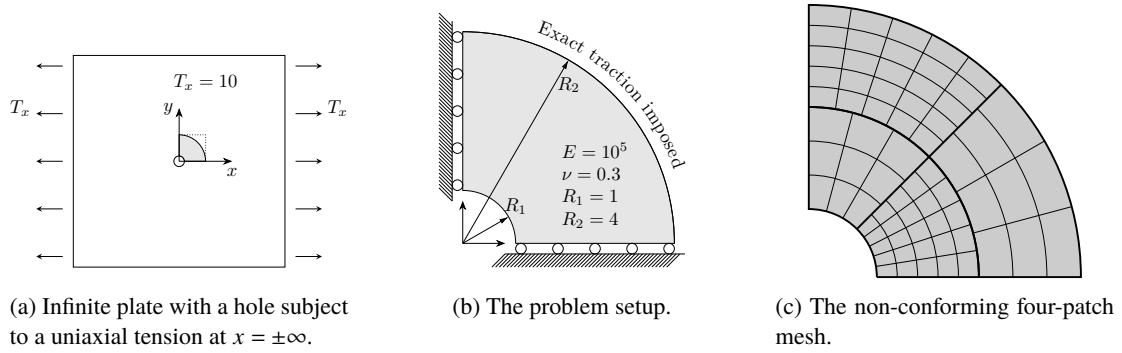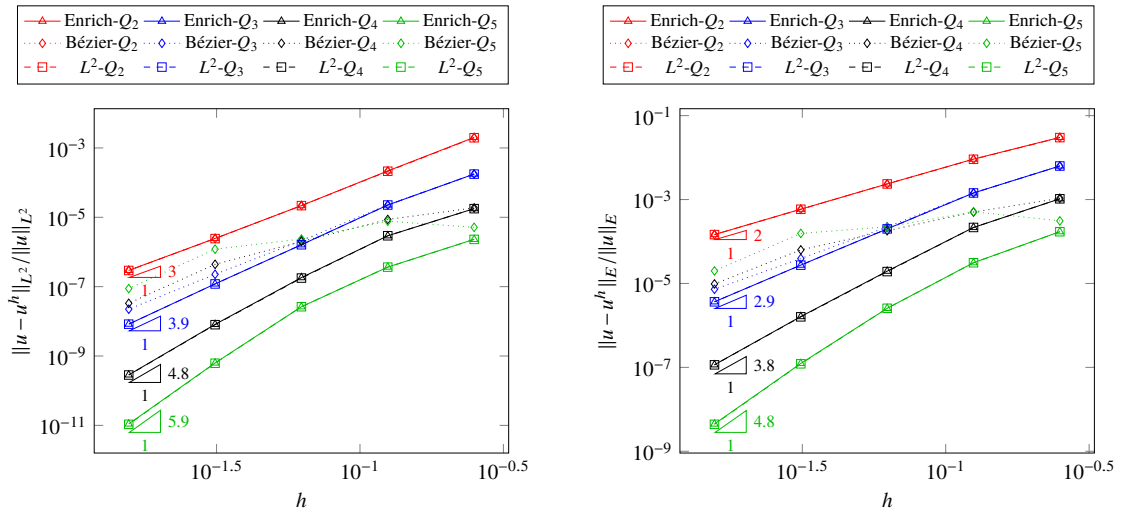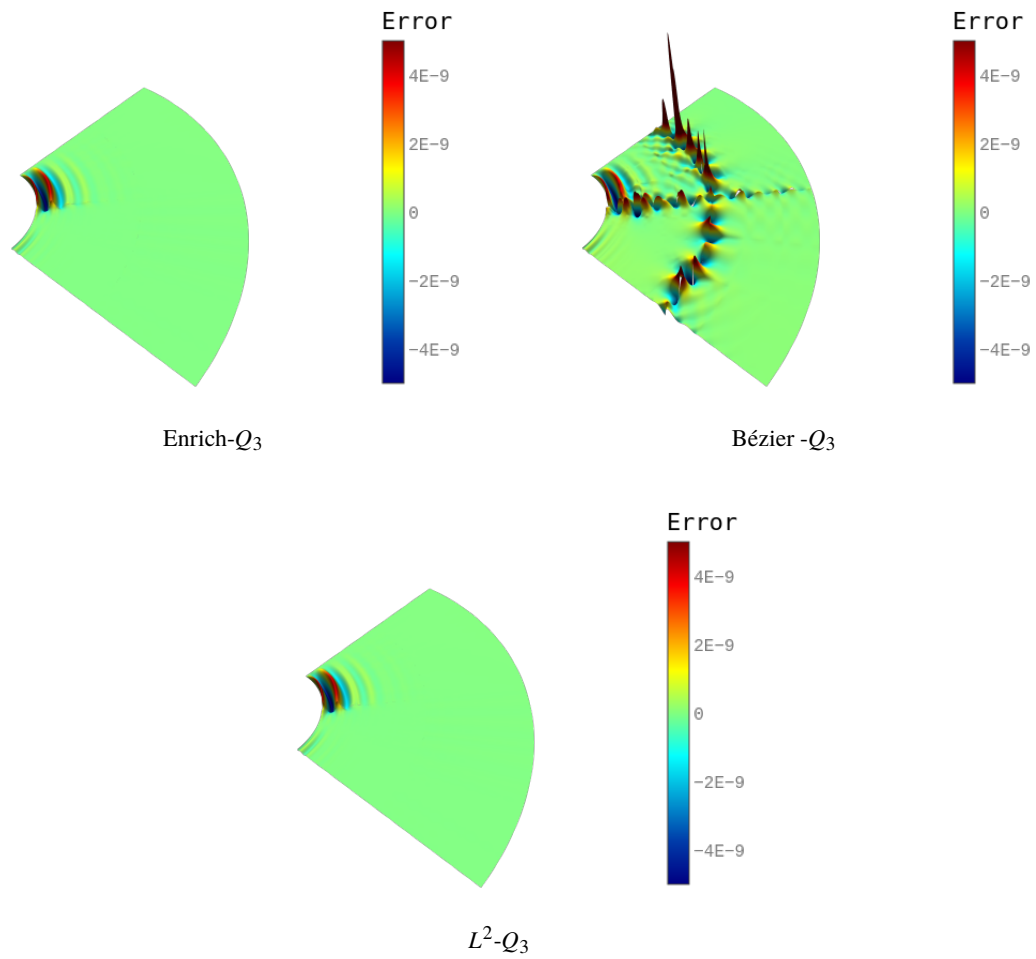
(a) Infinite plate with a hole subject to a uniaxial tension at $x = \pm\infty$.

(b) The problem setup.

(c) The non-conforming four-patch mesh.

Figure 19: The infinite plate with a hole problem.

Figure 20: Convergence plots for the problem described in Section 8.2. On the left, the error measured in the L^2 norm. On the right, the error measured in the energy semi-norm.

Enrich-Q_3

Bézier -Q_3

L^2-Q_3

Figure 21: Error plots for the linear elasticity problem on a four-patch domain ($p = 3$, three uniform mesh refinements).

8.3 The biharmonic problem

We consider a homogeneous biharmonic problem over the domain $[0,1] \times [0,1]$ and a manufactured solution

$$u(x,y) = \sin(2\pi x)^2 \sin(2\pi y)^2. \tag{102}$$
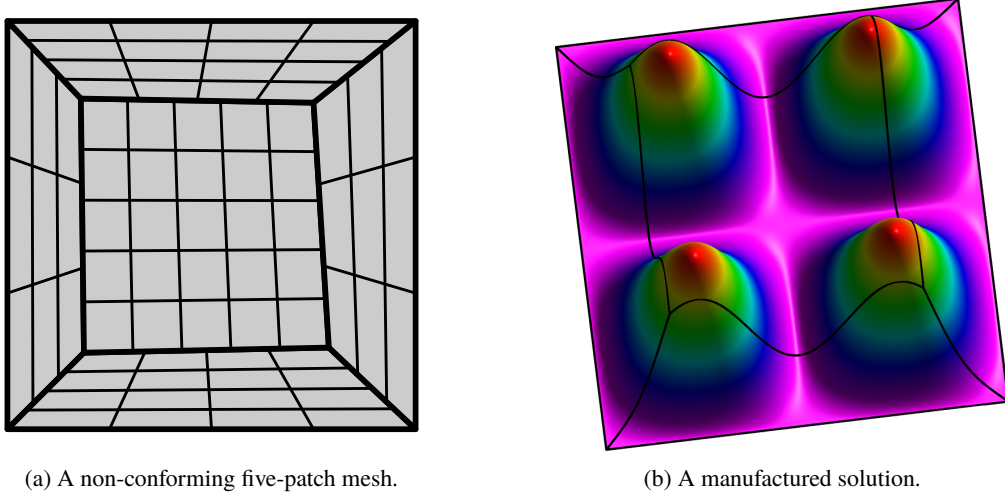
The problem setup is shown in Figure 22.

(a) A non-conforming five-patch mesh.

(b) A manufactured solution.

Figure 22: The biharmonic problem setup.

Error convergence plots for the biharmonic problem are shown in Figure 23. The enriched Bézier dual basis with $q = p - 2$ produces optimal results for $p = 2, 3, 4$ and the convergence plots are identical to those produced by the global dual basis. Note that the optimal convergence rate for quadratic basis functions is $O(h^2)$ in the L^2 norm for biharmonic problems. For the $p = 5$ case, we observe sub-optimal convergence for both the enriched and global dual basis and the most highly refined mesh in the L^2 norm. However, no sub-optimality is observed for the H^2 norm. This behavior indicates that the error occurs at certain digits of the floating point vector $\mathbf{U}^{\text{mortar}}$ (between the 7th and 10th digits for this case). We infer that the cause of this error is the poor conditioning of the stiffness matrix. In addition, previous studies [46] show that the growth rate of the condition number for the biharmonic problem is $O(-h^4)$, which is huge when compared with $O(-h^2)$ for the Poisson problem. This explains why the ill-conditioning of the biharmonic problem occurs much earlier than for the Poisson problem. We also attribute the slightly better performance of the enriched Bézier dual basis to their compact support and the robust construction algorithm (Algorithm 4). Again, the Bézier dual basis leads to sub-optimal behavior for higher-order elements.

Error plots for the cubic mesh after two uniform refinements are shown in Figure 24. Similar to second-order problems, the error plot for the enriched dual basis is identical to that of the global dual basis due to the absence of mismatched parameterizations along each intersection.

8.4 A Kirchhoff plate

The bending moments of a Kirchhoff plate are given by:

$$M_{xx} = -D\left(\frac{\partial^2 w}{\partial x^2} + \nu \frac{\partial^2 w}{\partial y^2}\right),$$
$$M_{yy} = -D\left(\frac{\partial^2 w}{\partial y^2} + \nu \frac{\partial^2 w}{\partial x^2}\right), \tag{103}$$
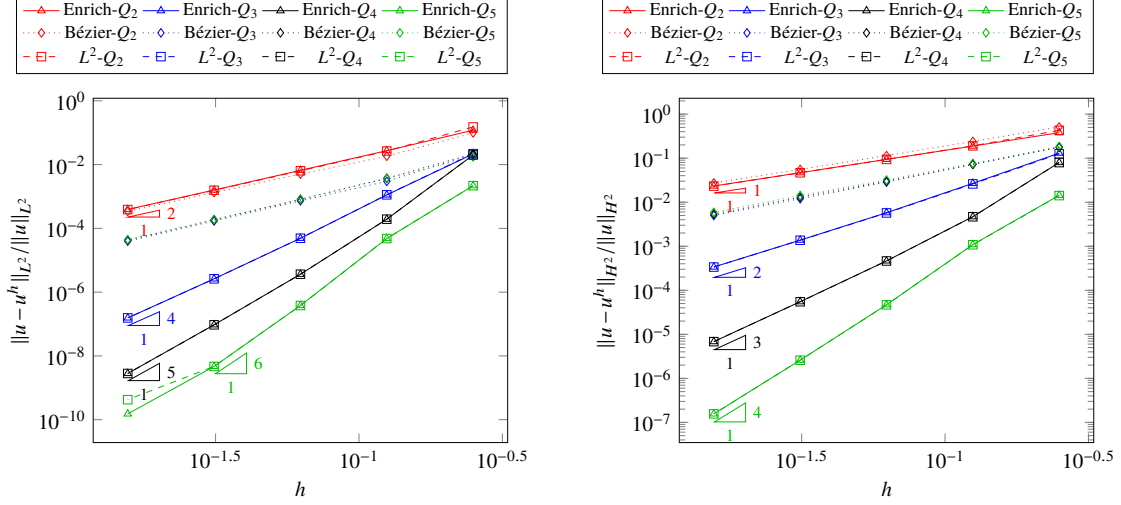$$M_{xy} = -D(1-\nu)\frac{\partial^2 w}{\partial xy},$$

31

Figure 23: Convergence plots for the problem described in Section 8.3. On the left, the error measured in the L^2 norm. On the right, the error measured in the H^2 norm.

where w is the vertical displacement, $D = \frac{Et^3}{12(1-\nu^2)}$, t is the thickness, E is the Young's modulus and ν is the Poisson's ratio. The governing equation of a Kirchhoff plate can be derived as

$$\frac{\partial^4 w}{\partial x^4} + \frac{\partial^4 w}{\partial x^2 y^2} + \frac{\partial^4 w}{\partial y^4} = \frac{q}{D} \tag{104}$$

where q is the pressure. In this benchmark, we consider a square plate with $L = 12$ subjected to a sinusoidal presure load of

$$q(x, y) = -\sin(\frac{\pi x}{L})\sin(\frac{\pi y}{L}). \tag{105}$$

We also adopt $t = 0.375$, $E = 4.8 \times 10^5$ and $\nu = 0.38$. The analytical solution is given by

$$w(x, y) = -\frac{L^4}{4D\pi^4}\sin(\frac{\pi x}{L})\sin(\frac{\pi y}{L}). \tag{106}$$

The geometry, discretization and the analytical solution of vertical displacement are shown in Figure 25. Note that the green intersection has a non-matching parameterization, whereas the red curves are coupled in a non-comforming fashion.

Convergence behaviors of w, M_{xx} and M_{xy} are studied in Figure 26. As can be seen, both the enriched Bézier dual basis and the global dual basis yield optimal results for all polynomial orders in all three measures. As for the biharmonic problem, ill-conditioning for the last refinement of $p = 5$ is observed in the L^2 norm whereas convergences of errors in M_{xx} and M_{xy} are still optimal. Due to the presence of a non-matching parameterized intersection, vertical shifts in the error plots of the enriched Bézier dual basis have been observed for higher order elements ($p = 4, 5$). Again, the Bézier dual basis generates sub-optimal results.

Error plots of err $= u_x - u_x^h$ for the simply supported Kirchhoff plate problem are given in Figure 27. For the enriched Bézier dual basis and the global dual basis, no oscillation are observed on the curved intersecitons, however, errors evolve along the non-matching parameterized intersection. Additionally, the influence of the non-matching intersection is more significant for the enriched Bézier dual basis. For the case of the Bézier dual basis, the consistency error is much higher and propagates into all patches.

8.5 The Cahn-Hilliard equation

In this benchmark, we verify the robustness of the dual mortar method and the enriched Bézier dual basis on a fourth-order non-linear dynamic problem – the Cahn-Hilliard equation. The Cahn-Hilliard equation was originally

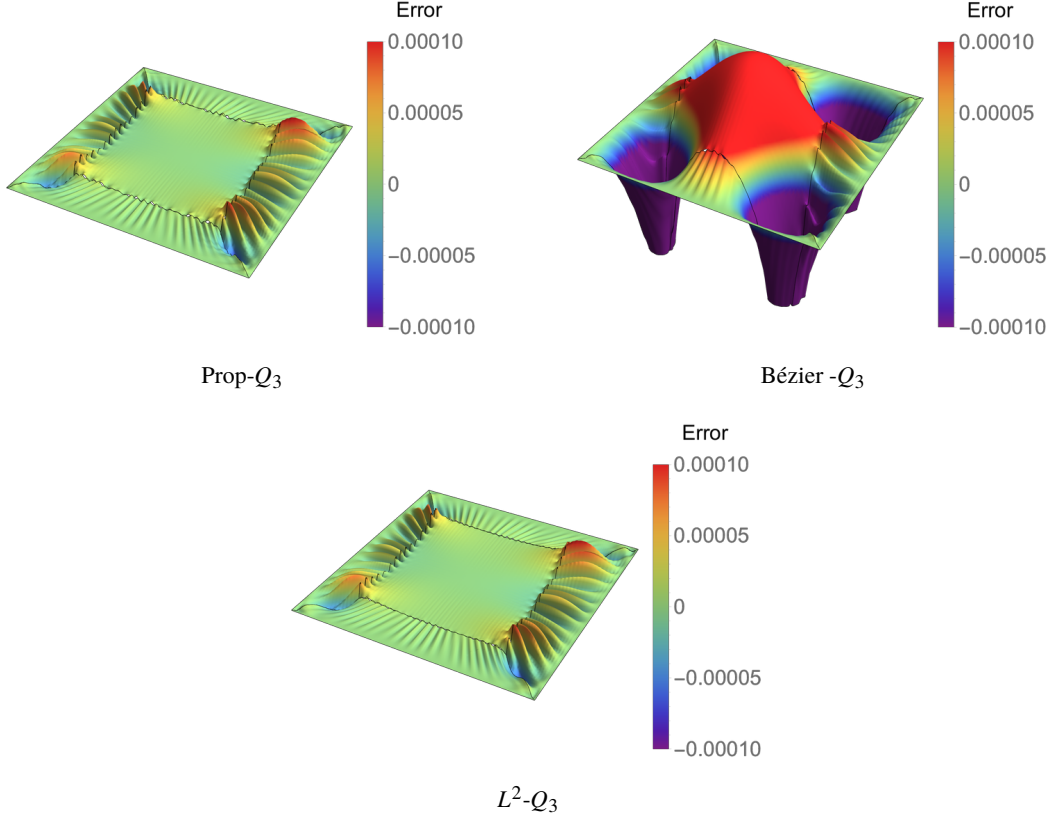Prop-Q_3 Bézier -Q_3

L^2-Q_3

Figure 24: Error plots for the biharmonic problem on a five-patch domain ($p = 3$, two uniform mesh refinements).

derived to model the spinodal decomposition of binary mixtures. Taking the concentration u of one of the mixture's components as a phase-field parameter, the governing equation over an infinite domain can be stated as

$$\frac{\partial u}{\partial t} = \nabla \cdot (M(u)\nabla(\mu(u) - \lambda \Delta u)) \text{ in } \Omega \times [0, T],$$

$$u(\mathbf{x}, 0) = u_0(\mathbf{x}) \text{ in } \Omega \tag{107}$$

where $M(u)$ is the mobility, $\mu(u)$ represents the chemical potential of a regular solution in the absence of phase interfaces and λ is a positive constant such that $\sqrt{\lambda}$ represents the length scale of the problem. In this benchmark, we study the concentration distribution over a two-dimensional domain with different initial and boundary conditions. We consider

$$M(u) = Du(1-u), \tag{108}$$

$$\mu(u) = 3\alpha\left(\frac{1}{2\theta}\log\frac{u}{1-u} + 1 - 2u\right), \tag{109}$$

and adopt the following values: $\alpha = 3000$, $D = 1$, $\lambda = 1$ and $\theta = 1.5$. The weak form is stated as follows: find $u \in \mathcal{U}$ such that $\forall v \in \mathcal{V}$

$$\langle\frac{\partial u}{\partial t}, v\rangle_\Omega + \langle M(u)\nabla\mu(u) + \nabla M(u)\Delta u, \nabla v\rangle_\Omega + \langle M(u)\Delta u, \Delta v\rangle_\Omega = 0, \tag{110}$$

where $\mathcal{U}$ and $\mathcal{V}$ are suitable function spaces.

To achieve an optimal ratio of high-frequency and low-frequency dissipation, we adopt the first-order generalized-α method [17, 36] as the temporal discretization scheme. In each time step, we require that the nonlinear residual decreases to 10^{-4} of its initial value. For the sake of computational efficiency, we adopt the adaptive time stepping scheme introduced by Gómez et al. in [28]. This adaptive time stepping scheme takes advantage of the fact that the generalized-α method contains the backward Euler method as a special case, and use the relative error between the

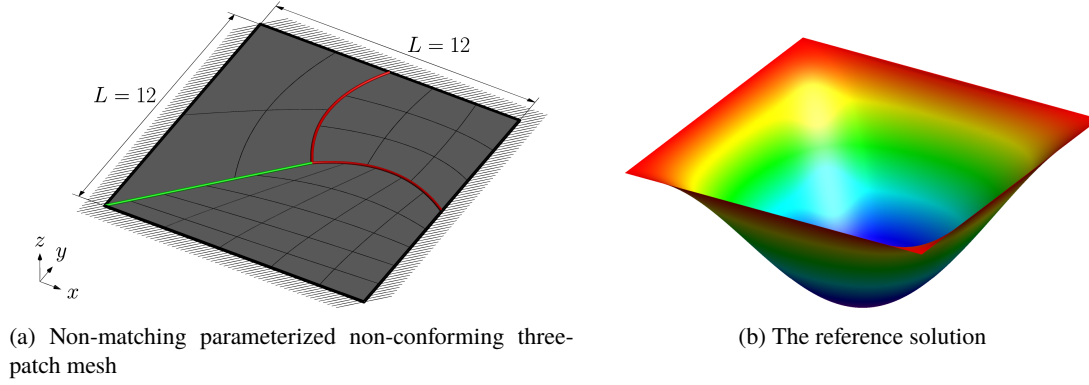(a) Non-matching parameterized non-conforming three-patch mesh

(b) The reference solution

Figure 25: The decomposition and discretization of the domain $[0,1] \times [0,1]$ and the reference solution that satisfies $u = 0$ on $\partial\Omega$ in Section 8.4. The non-matching parameterized interface is denoted by the green curve and the non-conforming interfaces are denoted by red curves.

solution from generalized-α method and the solution from the backward Euler method as an estimator of the current step size.

8.5.1 Stochastic concentration distribution

We first consider an initially stochastic concentration distribution over an infinite two-dimensional domain, as:

$$u_0(\mathbf{x}) = \bar{u} + r(\mathbf{x}), \tag{111}$$

where $\bar{u} = 0.63$ and r is a random variable with uniform distribution in the range $[-0.005, 0.005]$. The infinite domain can be described by a square domain $\Omega = [0,1] \times [0,1]$ with periodic boundary conditions. Hence, for this case, both $\mathcal{U}$ and $\mathcal{V}$ are in $H^2(\Omega)$ and satisfy periodic boundary condition. Taking into account that periodic boundary conditions are applied, it is anticipated that in the steady state only one circular inclusion will remain. To demonstrate the robustness of the dual mortar method and the enriched Bézier dual basis, we non-uniformly discretize the domain Ω into 64×64 quadratic elements, the periodic boundary condition is applied through the dual mortar method.

The mesh and the structural evolution of the concentration distribution are shown in Figure 28. Note that both the top/bottom and the left/right interfaces are non-matching parameterized. As can be seen, from its initial stochastic pattern, the concentration distribution evolves into two phases whose composition is determined by the minima of the bulk free energy. The process is dominated by the reduction of the number of $u = 0$ phases. Meanwhile, the characteristic length of the $u = 0$ phase is increased. Finally, the circular shape of the single inclusion is formed as a result of the bulk free energy minimization.

8.5.2 Linear concentration distribution

In the second case, we do not take $\bar{u}$ as a constant, but we vary it linearly with the horizontal spatial coordinate from 0.1 to 0.9. The domain $\Omega = [0,2] \times [0,2]$ is decomposed into four patches that are coupled non-conformingly. In addition, to show the compatibility of the coupling method with other types of boundary conditions, we consider

$$\frac{\partial u}{\partial \mathbf{n}} = 0, \quad \text{on } \partial\Omega. \tag{112}$$

The mesh and the structural evolution of the concentration distribution are shown in Figure 29. Four patches are discretized into 63×63, 65×65, 65×65 and 63×63 cubic elements, correspondingly. In this case, three morphologies are formed in different regions of the domain. On the left-hand side of the domain, the red phase nucleates into the blue one. The exact opposite occurs on the right-hand side. In the middle, where $u \approx 0.5$, we observe the striped pattern typical from spinodal decomposition. Whereas the nucleation process is dominated in the middle region, the structural evolution at the boundaries $x = 0$ and $x = 2$ hardly exists. Eventually, the interface develops into a straight line at $x = 1$, which is consistent with the behavior of the exact solution.
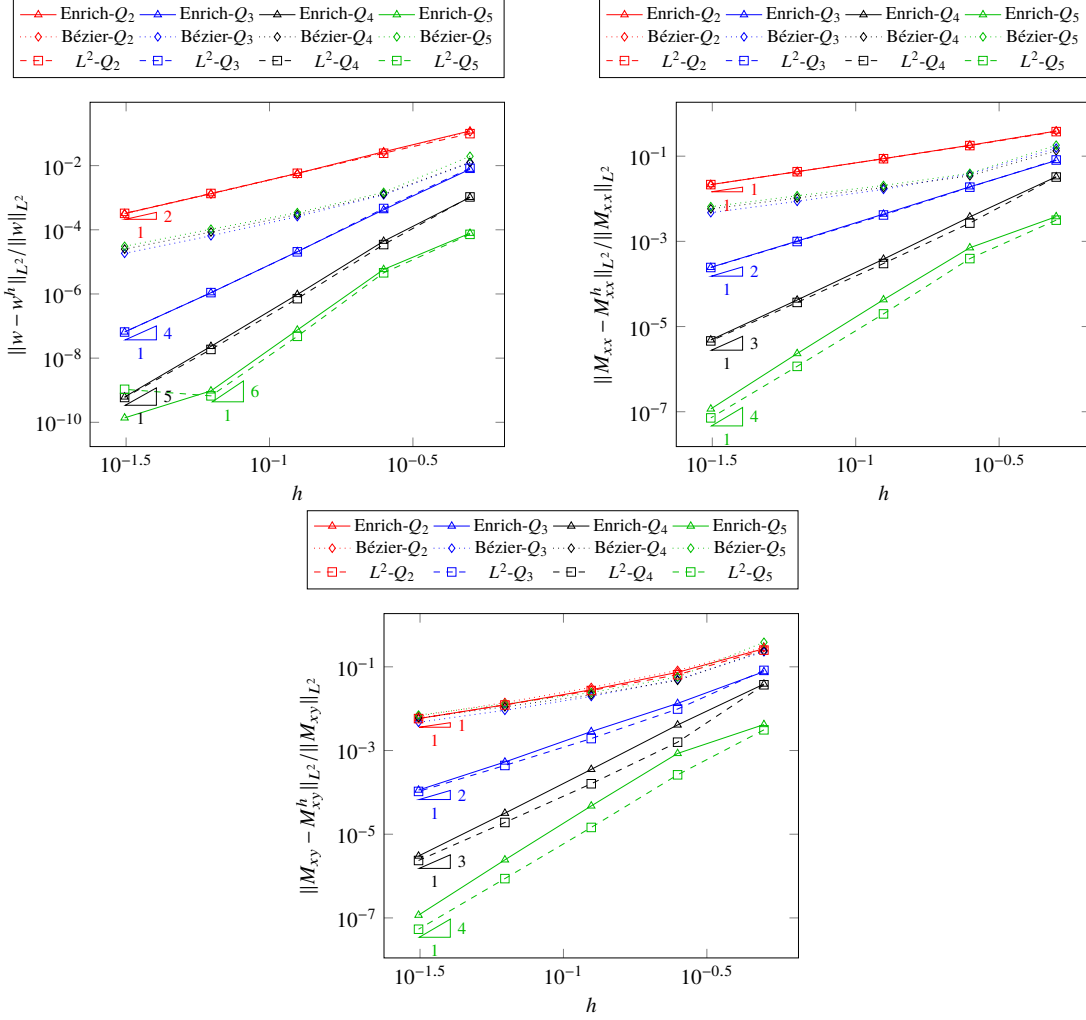
Figure 26: Convergence plots for the simply supported Kirchhoff plate in Section 8.4. Upper left: error of w measured in the L^2 norm. Upper right: error of M_{xx} measured in the L^2 norm. Bottom: error of M_{xy} measured in the L^2 norm.

In both cases, the convergence of Newton's method is achieved within 3 interations when $\Delta t < 5 \times 10^{-6}$ and 4 interations when $5 \times 10^{-6} \leq \Delta t < 1 \times 10^{-4}$ for both the generalized-α method and the backward Euler method. This is the same as for a simulation performed on one uniformly discretized patch. In addition, no influence on the time step size of the adaptive time stepping scheme has been observed. This confirms that the dual mortar method with the enriched Bézier dual basis does not negatively impact the convergence behavior of the residual correction loop and the overall robust performance when solving nonlinear problems.
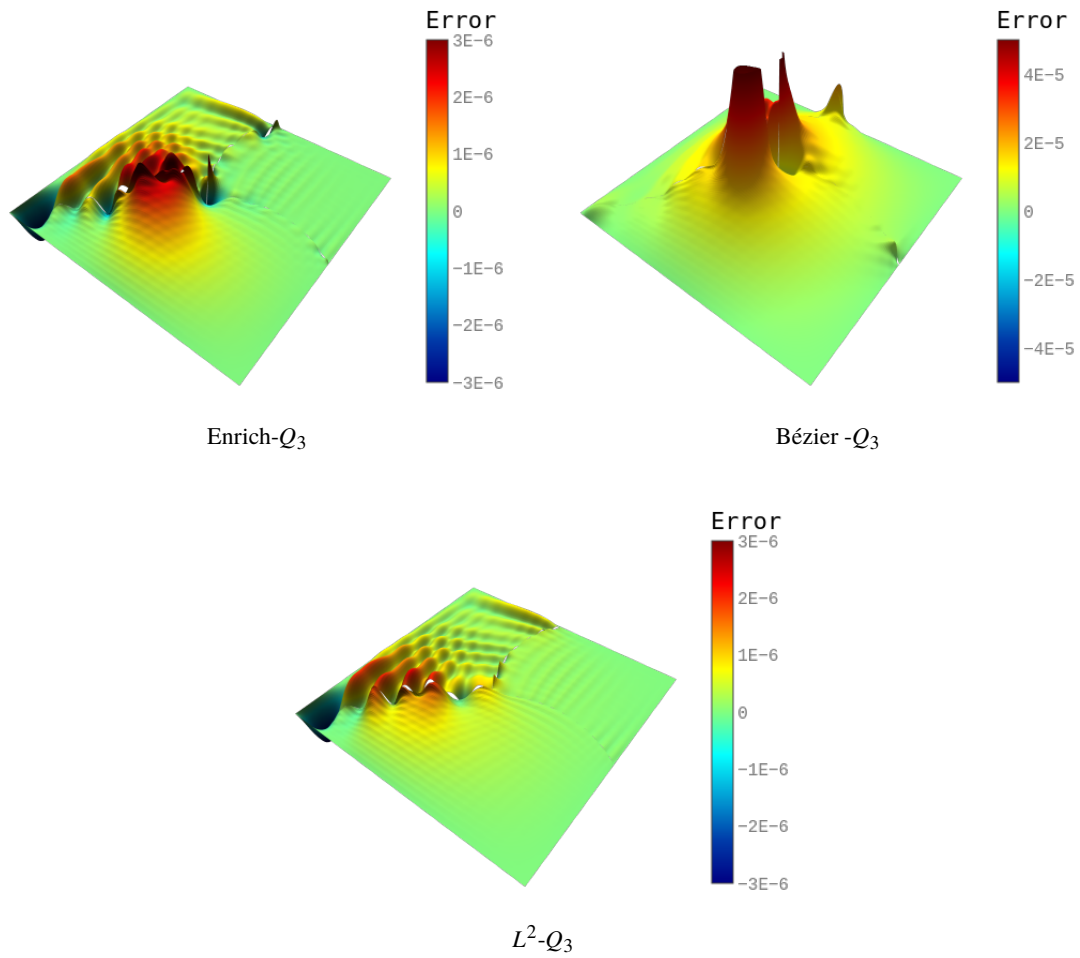
Enrich-Q_3

Bézier -Q_3

L^2-Q_3

Figure 27: Error plots of err $= u_x - u_x^h$ for the simply supported Kirchhoff plate problem on a three-patch domain ($p = 3$, two uniform mesh refinements).
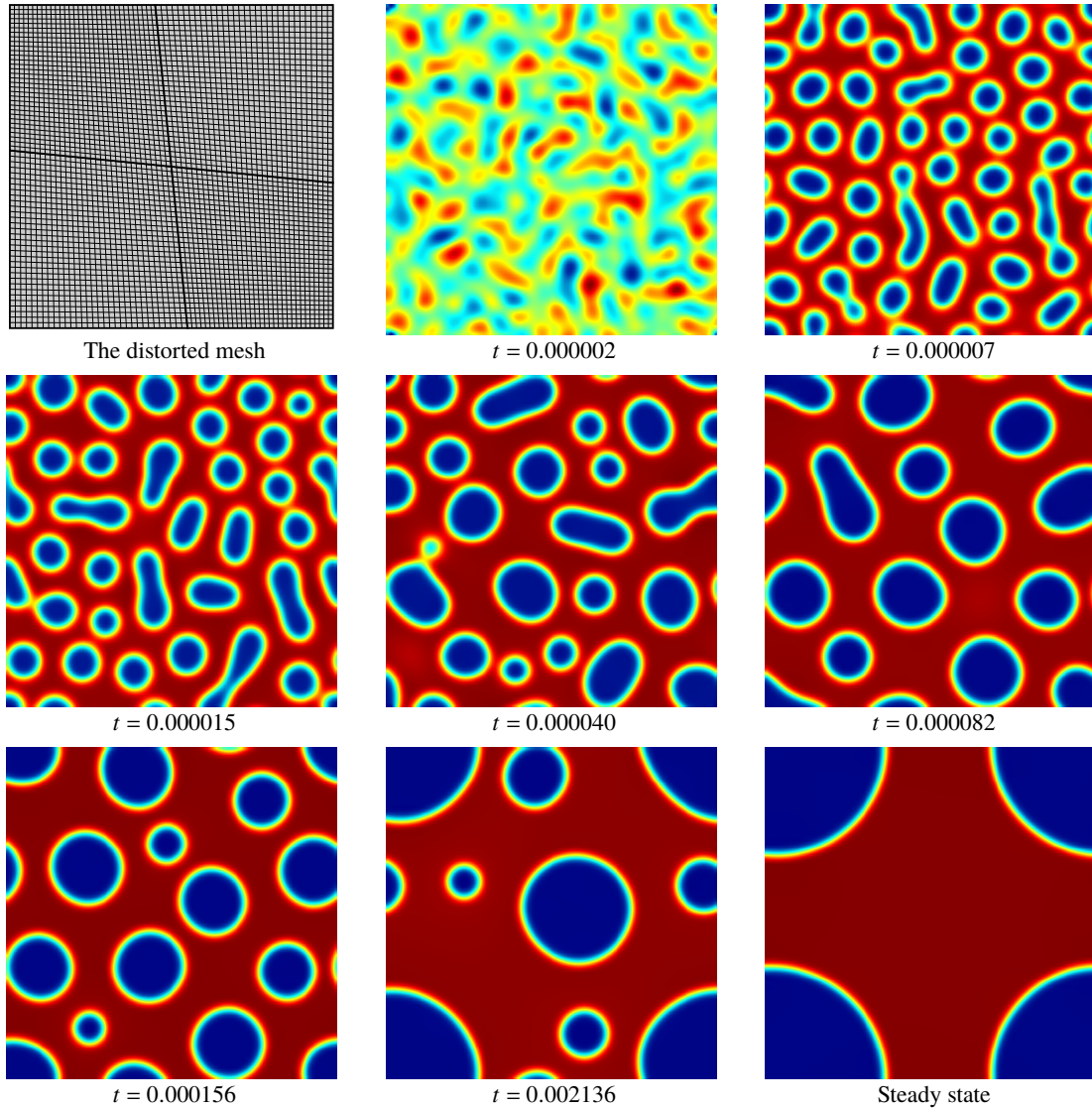
Figure 28: Temporal evolution of an initially stochastic concentration distribution into phases of different composition. The periodic boundary conditions are applied by the dual mortar method with the enriched Bézier dual basis. The computational domain is non-uniformly discretized, mesh lines at $\xi = 0.5$ and $\eta = 0.5$ are highlighted.
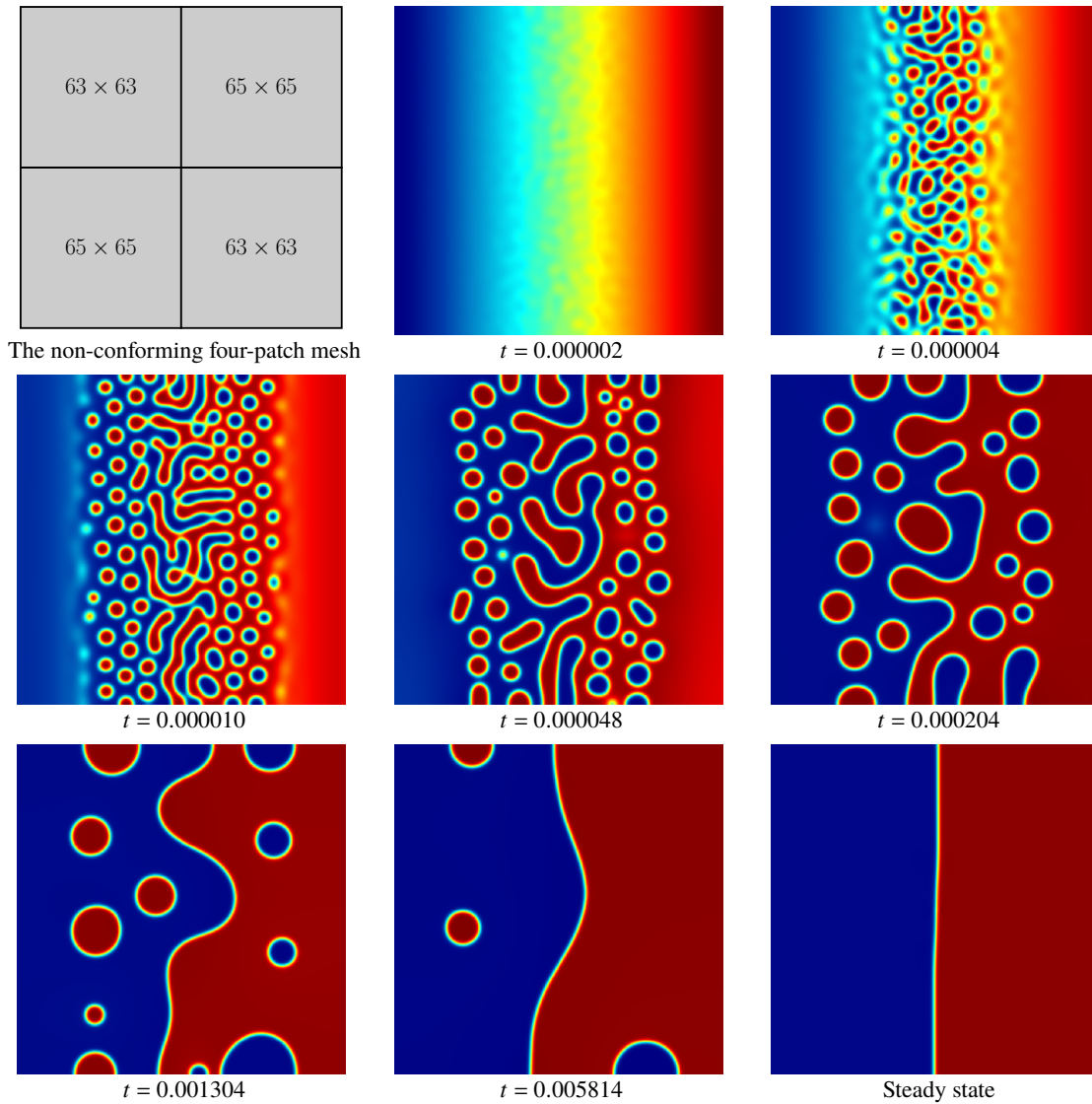
Figure 29: Temporal evolution of an initially linear concentration distribution with stochastic perturbation into two phases separated by a straight interface. The four-patch domain are coupled by the dual mortar method with the enriched Bézier dual basis.

9 Conclusion

In this paper, we develop an enrichment procedure to endow Bézier dual basis functions with optimal approximation power and deverlop dual mortar methods to solve second- and fourth-order problems. The cause of suboptimal convergence of the Bézier dual basis is due to the lack of polynomial reproduction. The enriched Bézier dual basis can reproduce polynomials up to a given degree at the expense of a slightly enlarged support. Owing to the locality of the dual basis, the linear system after static condensation remains sparse. The proposed enrichment approach is based on the formulation in Oswald et al. [51] with three significant improvements: (1) our approach is quadrature-free, (2) the conditioning is independent of the mesh size, and (3) it is posed in terms of Bézier extraction and projection. Hence, the assembly cost is minimized and overall solution robustness is improved.

In the context of fourth-order dual mortar formulations, we develop a parameterization-independent dual mortar suitable C^1 constraint that allows the biorthogonality between the dual basis functions and the corresponding primal spline basis functions to be extended to the discretized C^1 constraint matrix. Hence, the condensed stiffness matrix remains sparse if the dual basis functions are compactly supported.

The performance of the enriched dual basis is demonstrated through several challenging benchmark problems including second-order, fourth-order, linear, nonlinear, static and dynamic problems. The proposed dual basis demonstrates optimal convergence and yields compelling results, especially when compared to global and standard Bézier dual basis functions.

Finally, although the proposed enrichment procedure overcomes the suboptimality of the Bézier dual basis at the expense of a slightly enlarged support, in [44], Lamichhane developed dual basis functions that have the same support size as the nodal finite element basis functions and reproduce polynomials of degree $p - 1$. Hence, we believe there exists a superior formulation for smooth splines that can achieve the same performance without any influence on the support size.

References

[1] Andreas Apostolatos, Michael Breitenberger, Roland Wüchner, and Kai-Uwe Bletzinger. Domain decomposition methods and Kirchhoff-Love shell multipatch coupling in isogeometric analysis. In *Isogeometric Analysis and Applications 2014*, pages 73–101. Springer, 2015.

[2] Y. Bazilevs, V. M. Calo, J. A. Cottrell, J. A. Evans, T. J. R. Hughes, S. Lipton, M. A. Scott, and T. W. Sederberg. Isogeometric analysis using T-splines. *Computer Methods in Applied Mechanics and Engineering*, 199(5âĂŞ8):229–263, January 2010.

[3] Yuri Bazilevs, L Beirao da Veiga, J Austin Cottrell, Thomas J R Hughes, and Giancarlo Sangalli. Isogeometric analysis: approximation, stability and error estimates for h-refined meshes. *Mathematical Models and Methods in Applied Sciences*, 16(07):1031–1090, 2006.

[4] Yuri Bazilevs, Victor M Calo, Yongjie Zhang, and Thomas J R Hughes. Isogeometric fluid–structure interaction analysis with applications to arterial blood flow. *Computational Mechanics*, 38(4-5):310–322, 2006.

[5] Zakaria Belhachmi and Christine Bernardi. Resolution of fourth-order problems by the mortar element method. *Computer Methods in Applied Mechanics and Engineering*, 116(1):53–58, January 1994.

[6] David J Benson, Yuri Bazilevs, Emmanuel De Luycker, M C Hsu, M A Scott, T J R Hughes, and Ted Belytschko. A generalized finite element formulation for arbitrary basis functions: from isogeometric analysis to XFEM. *International Journal for Numerical Methods in Engineering*, 83(6):765–785, 2010.

[7] C. Bernardi, Y. Maday, and A. T. Patera. *Domain Decomposition by the Mortar Element Method*, chapter 17, pages 269–286. Springer Netherlands, Dordrecht, 1993.

[8] Christine Bernardi, Yvon Maday, and Francesca Rapetti. Basics and some applications of the mortar element method. *GAMM-Mitteilungen*, 28(2):97–123, November 2005.

[9] Michael J Borden, Thomas J R Hughes, Chad M Landis, and Clemens V Verhoosel. A higher-order phase-field model for brittle fracture: Formulation and analysis within the isogeometric analysis framework. *Computer Methods in Applied Mechanics and Engineering*, 273:100–118, 2014.

[10] Michael J Borden, Michael A Scott, John A Evans, and Thomas J R Hughes. Isogeometric finite element data structures based on Bézier extraction of NURBS. *International Journal for Numerical Methods in Engineering*, 87(1-5):15–47, 2011.

[11] Robin Bouclier, Jean-Charles Passieux, and Michel SalaÃijn. Development of a new, more regular, mortar method for the coupling of NURBS subdomains within a NURBS patch: Application to a non-intrusive local enrichment of NURBS patches. *Computer Methods in Applied Mechanics and Engineering*, 316:123–150, April 2017.

[12] Susanne Brenner and Ridgway Scott. *The Mathematical Theory of Finite Element Methods*. Springer Science & Business Media, December 2007.

[13] Ericka Brivadis, Annalisa Buffa, Barbara Wohlmuth, and Linus Wunderlich. Isogeometric mortar methods. *Computer Methods in Applied Mechanics and Engineering*, 284:292–319, February 2015.

[14] Daniel Burkhart, Bernd Hamann, and Georg Umlauf. Isogeometric finite element analysis based on Catmull-Clark: subdivision solids. In *Computer Graphics Forum*, volume 29, pages 1575–1584. Wiley Online Library, 2010.

[15] Edwin Catmull and James Clark. Recursively generated B-spline surfaces on arbitrary topological meshes. *Computer-aided design*, 10(6):350–355, 1978.

[16] Chiu Ling Chan, Cosmin Anitescu, and Timon Rabczuk. Isogeometric analysis with strong multipatch C^1-coupling. *Computer Aided Geometric Design*, 62:294–310, 2018.

[17] Jintai Chung and G M Hulbert. A time integration algorithm for structural dynamics with improved numerical dissipation: the generalized-α method. *Journal of applied mechanics*, 60(2):371–375, 1993.

[18] Annabelle Collin, Giancarlo Sangalli, and Thomas Takacs. Analysis-suitable G^1 multi-patch parametrizations for C^1 isogeometric spaces. *Computer Aided Geometric Design*, 47:93–113, October 2016.

[19] L Beirao da Veiga, Annalisa Buffa, D Cho, and G Sangalli. Isogeometric analysis using T-splines on two-patch geometries. *Computer methods in applied mechanics and engineering*, 200(21-22):1787–1803, 2011.

[20] L Beirao Da Veiga, Annalisa Buffa, Judith Rivas, and Giancarlo Sangalli. Some estimates for h–p–k-refinement in Isogeometric Analysis. *Numerische Mathematik*, 118(2):271–305, 2011.

[21] L Beirao Da Veiga, Annalisa Buffa, Giancarlo Sangalli, and Rafael Vázquez. Mathematical analysis of variational Isogeometric methods. *Acta Numerica*, 23:157–287, 2014.

[22] Carl De Boor. *On local linear functionals which vanish at all B-splines but one*. Mathematics Research Center, University of Wisconsin, 1975.

[23] Carl de Boor and GJ Fix. Spline approximation by quasiinterpolants. *Journal of Approximation Theory*, 8(1):19–45, 1973.

[24] M Dittmann, S Schuß, B Wohlmuth, and C Hesch. Weak c n coupling for multipatch isogeometric analysis in solid mechanics. *International Journal for Numerical Methods in Engineering*, 118(11):678–699, 2019.

[25] Charbel Farhat and Francois Xavier Roux. A method of finite element tearing and interconnecting and its parallel solution algorithm. *International Journal for Numerical Methods in Engineering*, 32(6):1205–1227, 1991.

[26] Gerald Farin, Josef Hoschek, and M S Kim. *Handbook of computer aided geometric design*. Elsevier, 2002.

[27] Rida T Farouki and VT Rajan. Algorithms for polynomials in Bernstein form. *Computer Aided Geometric Design*, 5(1):1–26, 1988.

[28] Héctor Gómez, Victor M Calo, Yuri Bazilevs, and Thomas J R Hughes. Isogeometric analysis of the Cahn–Hilliard phase-field model. *Computer methods in applied mechanics and engineering*, 197(49-50):4333–4352, 2008.

[29] L Greco, M Cuomo, and L Contrafatto. A reconstructed local B-bar formulation for isogeometric Kirchhoff–Love shells. *Computer Methods in Applied Mechanics and Engineering*, 332:462–487, 2018.

[30] Gaël Guennebaud, Benoît Jacob, et al. Eigen v3. http://eigen.tuxfamily.org, 2010.

[31] P A Guidault and Ted Belytschko. On the L^2 and the H^1 couplings for an overlapping domain decomposition method using lagrange multipliers. *International journal for numerical methods in engineering*, 70(3):322–350, 2007.

[32] Yujie Guo and Martin Ruess. NitscheâĂŹs method for a coupling of isogeometric thin shells and blended shell structures. *Computer Methods in Applied Mechanics and Engineering*, 284:881–905, February 2015.

[33] Peter Hansbo, Carlo Lovadina, Ilaria Perugia, and Giancarlo Sangalli. A lagrange multiplier method for the finite element solution of elliptic interface problems using non-matching meshes. *Numerische Mathematik*, 100(1):91–115, 2005.

[34] Thomas Horger, Alessandro Reali, Barbara Wohlmuth, and Linus Wunderlich. A hybrid isogeometric approach on multi-patches with applications to Kirchhoff plates and eigenvalue problems. *Computer Methods in Applied Mechanics and Engineering*, 348:396–408, 2019.

[35] T. J. R. Hughes, J.A. Cottrell, and Y. Bazilevs. Isogeometric analysis: CAD, finite elements, NURBS, exact geometry and mesh refinement. *Computer Methods in Applied Mechanics and Engineering*, 194(39):4135 – 4195, 2005.

[36] Kenneth E Jansen, Christian H Whiting, and Gregory M Hulbert. A generalized-α method for integrating the filtered Navier–Stokes equations with a stabilized finite element method. *Computer methods in applied mechanics and engineering*, 190(3-4):305–319, 2000.

[37] Bert Jüttler. The dual basis functions for the Bernstein polynomials. *Advances in Computational Mathematics*, 8(4):345–352, 1998.

[38] Mario Kapl, Florian Buchegger, Michel Bercovier, and Bert JÃijttler. Isogeometric analysis with geometrically continuous functions on planar multi-patch geometries. *Computer Methods in Applied Mechanics and Engineering*, 316:209–234, April 2017.

[39] Mario Kapl, Vito Vitrih, Bert JÃijttler, and Katharina Birner. Isogeometric analysis with geometrically continuous functions on two-patch geometries. *Computers & Mathematics with Applications*, 70(7):1518–1538, October 2015.

[40] J Kiendl, Y Bazilevs, M C Hsu, R Wüchner, and K U Bletzinger. The bending strip method for isogeometric analysis of Kirchhoff–Love shell structures comprised of multiple patches. *Computer Methods in Applied Mechanics and Engineering*, 199(37-40):2403–2416, 2010.

[41] J Kiendl, K U Bletzinger, J Linhard, and R Wüchner. Isogeometric shell analysis with Kirchhoff–Love elements. *Computer Methods in Applied Mechanics and Engineering*, 198(49-52):3902–3914, 2009.

[42] Josef Kiendl, Ming Chen Hsu, Michael CH Wu, and Alessandro Reali. Isogeometric Kirchhoff–Love shell formulations for general hyperelastic materials. *Computer Methods in Applied Mechanics and Engineering*, 291:280–303, 2015.

[43] Hyun Jung Kim, Yu Deok Seo, and Sung Kie Youn. Isogeometric analysis for trimmed CAD surfaces. *Computer Methods in Applied Mechanics and Engineering*, 198(37-40):2982–2995, 2009.

[44] Bishnu Lamichhane and Barbara Wohlmuth. Biorthogonal bases with local support and approximation properties. *Mathematics of Computation*, 76(257):233–249, 2007.

[45] Bishnu Prasad Lamichhane and Barbara I Wohlmuth. Higher order dual lagrange multiplier spaces for mortar finite element discretizations. *Calcolo*, 39(4):219–237, 2002.

[46] Zi Cai Li, Hung Tsai Huang, and Jin Huang. Effective condition number of the Hermite finite element methods for biharmonic equations. *Applied Numerical Mathematics*, 58(9):1291–1308, 2008.

[47] C. Loop. Smooth subdivision surfaces based on triangles. *Master's Thesis, University of Utah, Department of Mathematics*, 1987.

[48] Di Miao, Michael J. Borden, Michael A. Scott, and Derek C. Thomas. Bézier B-bar projection. *Computer Methods in Applied Mechanics and Engineering*, 335:273 – 297, 2018.

[49] Thien Nguyen, Keçstutis Karčiauskas, and Jörg Peters. A comparative study of several classical, discrete differential and isogeometric methods for solving poissonâĂŹs equation on the disk. *Axioms*, 3(2):280–299, 2014.

[50] Vinh Phu Nguyen, Pierre Kerfriden, Marco Brino, StÃľphane P. A. Bordas, and Elvio Bonisoli. NitscheâĂŹs method for two and three dimensional NURBS patch coupling. *Computational Mechanics*, 53(6):1163–1182, June 2014.

[51] Peter Oswald and Barbara Wohlmuth. On polynomial reproduction of dual FE bases. In *Thirteenth international conference on domain decomposition methods*, pages 85–96, 2001.

[52] Qing Pan, Guoliang Xu, Gang Xu, and Yongjie Zhang. Isogeometric analysis based on extended Loop's subdivision. *Journal of Computational Physics*, 299:731–746, 2015.

[53] Jörg Peters. Joining smooth patches around a vertex to form a C^k surface. *Computer Aided Geometric Design*, 9(5):387–411, 1992.

[54] Jörg Peters. Constructing C^1 surfaces of arbitrary topology using biquadratic and bicubic splines. In *Designing Fair Curves and Surfaces: Shape Quality in Geometric Modeling and Computer-Aided Design*, pages 277–293. SIAM, 1994.

[55] Jörg Peters and Ulrich Reif. *Subdivision surfaces*. Springer, 2008.

[56] Les Piegl and Wayne Tiller. *The NURBS book*. Springer Science & Business Media, 2012.

[57] Beatrice Riviere. *Discontinuous Galerkin methods for solving elliptic and parabolic equations: theory and implementation*. SIAM, 2008.

[58] Robert Schmidt, Roland Wüchner, and Kai Uwe Bletzinger. Isogeometric analysis of trimmed NURBS geometries. *Computer Methods in Applied Mechanics and Engineering*, 241:93–111, 2012.

[59] S Schuß, M Dittmann, B Wohlmuth, S Klinkel, and C Hesch. Multi-patch isogeometric analysis for Kirchhoff–Love shell elements. *Computer Methods in Applied Mechanics and Engineering*, 349:91–116, 2019.

[60] Michael A Scott, Michael J Borden, Clemens V Verhoosel, Thomas W Sederberg, and Thomas J R Hughes. Isogeometric finite element data structures based on Bézier extraction of T-splines. *International Journal for Numerical Methods in Engineering*, 88(2):126–156, 2011.

[61] Michael A Scott, Robert N Simpson, John A Evans, Scott Lipton, Stephane PA Bordas, Thomas J R Hughes, and Thomas W Sederberg. Isogeometric boundary element analysis using unstructured T-splines. *Computer Methods in Applied Mechanics and Engineering*, 254:197–221, 2013.

[62] Thomas W. Sederberg, Jianmin Zheng, Almaz Bakenov, and Ahmad Nasri. T-splines and T-NURCCs. In *ACM SIGGRAPH 2003 Papers*, SIGGRAPH '03, pages 477–484, New York, NY, USA, 2003. ACM.

[63] Derek C Thomas, Michael A Scott, John A Evans, Kevin Tew, and Emily J Evans. Bézier projection: a unified approach for local projection and quadrature-free refinement and coarsening of NURBS and T-splines with particular application to isogeometric design and analysis. *Computer Methods in Applied Mechanics and Engineering*, 284:55–105, 2015.

[64] Deepesh Toshniwal, Hendrik Speleers, and Thomas J R Hughes. Smooth cubic spline spaces on unstructured quadrilateral meshes with particular emphasis on extraordinary points: Geometric design and isogeometric analysis considerations. *Computer Methods in Applied Mechanics and Engineering*, 327:411–458, 2017.

[65] Clemens V Verhoosel, Michael A Scott, Rene De Borst, and Thomas J R Hughes. An isogeometric approach to cohesive zone modeling. *International Journal for Numerical Methods in Engineering*, 87(1-5):336–360, 2011.

[66] Xiaodong Wei, Yongjie Zhang, Thomas J R Hughes, and Michael A Scott. Truncated hierarchical Catmull–Clark subdivision with local refinement. *Computer Methods in Applied Mechanics and Engineering*, 291:1–20, 2015.

[67] Xiaodong Wei, Yongjie Jessica Zhang, Thomas J R Hughes, and Michael A Scott. Extended truncated hierarchical Catmull–Clark subdivision. *Computer Methods in Applied Mechanics and Engineering*, 299:316–336, 2016.

[68] Barbara I Wohlmuth. A mortar finite element method using dual spaces for the lagrange multiplier. *SIAM journal on numerical analysis*, 38(3):989–1012, 2000.

[69] Linus Wunderlich, Alexander Seitz, Mert Deniz Alaydın, Barbara Wohlmuth, and Alexander Popp. Biorthogonal splines for optimal weak patch-coupling in isogeometric analysis with applications to finite deformation elasticity. *Computer Methods in Applied Mechanics and Engineering*, 346:197–215, 2019.

[70] Gang Xu, Bernard Mourrain, Régis Duvigneau, and André Galligo. Parameterization of computational domain in isogeometric analysis: methods and comparison. *Computer Methods in Applied Mechanics and Engineering*, 200(23-24):2021–2031, 2011.

[71] Gang Xu, Bernard Mourrain, André Galligo, and Timon Rabczuk. High-quality construction of analysis-suitable trivariate NURBS solids by reparameterization methods. *Computational Mechanics*, 54(5):1303–1313, 2014.

[72] Z Zou, M A Scott, M J Borden, D C Thomas, W Dornisch, and E Brivadis. Isogeometric Bézier dual mortaring: Refineable higher-order spline dual bases and weakly continuous geometry. *Computer Methods in Applied Mechanics and Engineering*, 333:497–534, 2018.